TITLE

The Italian contribution to the Synoptic Arctic Survey programme: the 2021 CASSANDRA cruise (LB21) through the Greenland Sea Gyre along the 75°N transect

AUTHORS

Manuel Bensi[1*], Giuseppe Civitarese[1], Diego Borme[1], Carmela Caroppo[2], Gabriella Caruso[3], Federica Cerino[1], Franco Decembrini[3], Alessandra de Olazabal[1], Tommaso Diociauti[1], Michele Giani[1], Vedrana Kovacevic[1], Martina Kralj[1], Angelina Lo Giudice[3], Giovanna Maimone[3], Marina Monti[1], Maria Papale[3], Luisa Patrolecco[5], Elisa Putelli[1], Alessandro Ciro Rappazzo[3], Federica Relitti[1], Carmen Rizzo[3,4], Francesca Spataro[5], Valentina Tirelli[1], Clara Turetta[6], Maurizio Azzaro[3]

[1] National Institute of Oceanography and Applied Geophysics, OGS, Trieste, Italy

[2] Water Research Institute, National Research Council, CNR-IRSA, Taranto, Italy

[3] Institute of Polar Sciences, National Research Council, CNR-ISP, Messina, Italy

[4] Stazione Zoologica Anton Dohrn, Sicily Marine Centre, SZN-SMC, Messina, Italy

[5] Institute of Polar Sciences, National Research Council, CNR-ISP, Rome, Italy

[6] Institute of Polar Sciences, National Research Council, CNR-ISP, Venice, Italy

Correspondence to: (mbensi@ogs.it)

ABSTRACT

In September 2021, as part of the Italian Arctic research programme, a multidisciplinary cruise along the 75th parallel north through the Greenland Sea Gyre was conducted aboard the Italian icebreaker Laura Bassi as part of the CASSANDRA project, which also contributed to the Synoptic Arctic Survey (SAS) 2020/22. The cruise took place during the period of the lowest summer sea ice extent ever measured. The data show strong horizontal gradients with temperatures between 1.5 °C and 9.0 °C and salinity between 30 and 35. Warm and salty Atlantic Water (AW, $\theta > 3.0$ °C, S around 35) dominates on the eastern side of the transect in the upper 500 m with surface temperatures of 4.5–9.0 °C, while Polar Water (PW, $\theta < 0$ °C, S < 33) occupies the surface layer (50–80 m) in the west. The intermediate layer (100–500 m) consists of mixed water, and below 500 m the deep water of the Greenland Sea and the Norwegian Sea predominates. The oxygen enrichment is higher in the intermediate layers, while the values in deep layers and western regions are lower (< 300 µmol kg^{-1}). A stratified upper layer (30–50 m deep) with low surface nutrients, especially nitrate, is observed, while an accumulation of silicate occurs in deep water masses. The surface water in the eastern part of the transect has high pH$_T$ and total alkalinity values due to photosynthesis and the presence of salty AW, while the fresh PW in the west has a lower alkalinity. Respiratory activity and organic matter concentrations (particulate/dissolved organic carbon) vary horizontally at the surface, decrease with depth, and increase slightly near the seafloor. A west-east gradient is also observed for δ^{18}O and δD, with the ratios indicating the influence of freshwater at the surface near the Greenland coast. The abundance of prokaryotes decreases from the photic zone

(< 100 m depth) to the sea floor. Carbohydrates and carboxylic acids are identified as well-utilised polymers at every station and in every layer. Overall, the microbial enzyme patterns show a decrease from the surface to deeper layers, with some hotspots of metabolic activity at 20-40 m and in the aphotic layer. The enzyme patterns vary spatially, with activity peaks at the ends and in the middle of the transect. Phytoplankton biomass, expressed as chlorophyll-a, varies across the transect, with higher values at the westernmost and easternmost stations. The micro-phytoplankton fraction dominates in PW, while the nano-phytoplankton fraction predominates in AW, even at the interface between the two water masses. Data of phytoplankton communities show low abundances and a dominance of nano-sized organisms, with diatoms being more abundant in the western part. Microzooplankton represents an important fraction of the planktonic community in this area, with tintinnids being the most important groups along the transect. Micrometazoans and aloricate ciliates are more abundant in the AW, resulting in higher biomass values at the eastern stations. Copepods are the most abundant mesozooplanktonic taxon both at the surface and in the upper 100 m water layer (97% and 94% of total mesozooplankton abundance, respectively), mainly represented by the genus *Calanus*.

The data are publicly available at the Italian Arctic Data Centre (IADC), see section Data availability.

1 INTRODUCTION

The Greenland Sea, in the north Atlantic, is a region of deep ocean convection that contributes to the Atlantic Meridional Overturning (AMOC) and the exchange of water masses between the Atlantic and Arctic Oceans. Its sensitivity to climate change remains uncertain, as the ecosystems of the subarctic Atlantic are particularly sensitive to global warming (Whitt, 2023). In fact, the Greenland Sea serves also as a hub for heat, salts, nutrients, carbon, and organisms between the Arctic, subarctic, and lower latitudes. Arctic and subarctic regions have experienced warming twice as fast as global warming over the past 50 years (Rantanen et al., 2022). This has led to significant environmental changes, including increasing wetness, reduced sea ice thickness and coverage, changes in snow cover, thawing of permafrost, and melting of the Greenland ice sheet (Carmack et al., 2015; Polyakov et al., 2017, 2023; Babb et al., 2023). These changes have created a positive feedback loop known as "Arctic amplification" which is likely to intensify in the future. Despite its crucial role in the global climate system, the Arctic Ocean remains poorly understood due to its remote location, harsh weather, and seasonal ice cover. The Arctic Ocean receives heat through the inflow of Atlantic Water (AW, with Temperature (T) > 0 °C). AW flows northward transported by the Norwegian Atlantic Current (NAC) and the West Spitsbergen Current (WSC) along the eastern slope of the North Atlantic and crosses the Greenland Sea and Fram Strait, where it is partly deflected by the local circulation (Fig. 1). On the other hand, the Arctic outflow of Polar Water (PW, T < 0 °C), together with the sea ice export from the Arctic, is driven by the East Greenland Current (EGC, Chatterjee et al., 2018). Greenland freshwater flux shows a large seasonal variation, with peaks in July (4-6 times higher than in winter), but also consistent increase since the 2000s (Dukhovskoy et al., 2019). Changes in annual and multi-year sea ice trends are also an important factor to consider when analysing the physical and biogeochemical conditions in the Greenland Sea. Sea ice extent and thickness in the Arctic regions have continuously decreased over the last four decades, and significant changes have also been observed in the Fram Strait since 2015 (de Steur et al., 2023). Since 2020, however, sea ice extent in the Fram Strait and marginal seas has shown a

81 slight recovery in seasonal winter maxima (Onarheim et al., 2024). Open-ocean convection also
82 occurs in the Greenland Sea during winter seasons. It is thought to represent a significant proportion
83 of dense water production for the regions, even though a large variability in this process has been
84 observed in recent decades, including changes in the depth of convection (Simpkins, 2019; Brakstad
85 et al., 2019). Overall, the predominant atmospheric conditions over the Arctic are characterised by
86 the presence of high pressure (i.e., Polar High) over the western Arctic and low pressure over the
87 Siberian region, which trigger the main anticyclonic wind regime. However, after 2007 a secondary
88 dipole, characterised by higher sea level pressure over the Beaufort Gyre and the Canadian
89 Archipelago along with lower sea level pressure over the Siberian Arctic, became dominantly
90 positive, favouring reduced flows into the Arctic through the Fram Strait along with enhanced
91 inflows through the Barents Sea Opening (Polyakov et al., 2023). Consequently, from 2007 to 2021,
92 the predominant cyclonic atmospheric regime over the Arctic Ocean pushed large amounts of
93 freshwater from the Siberian shelves into the Beaufort Gyre (Polyakov et al., 2023).

94 The cyclonic Greenland Sea Gyre (GSG) in the central Greenland Sea, which is mainly driven by
95 large-scale cyclonic winds, contributes to the regulation of the inflow and outflow of AW and PW
96 between the Atlantic and Arctic Oceans (Chatterjee et al., 2018). The GSG, and the North Atlantic
97 subpolar gyre (SPG), south of Iceland, have large implications for the large-scale changes in the
98 subpolar and polar marine environment. A strong GSG triggers a northwestward shift of the
99 subpolar front, which intensifies the poleward transport of Atlantic water towards the Fram Strait,
100 Barents Sea and Arctic Ocean (Chatterjee et al., 2018). In contrast, a weak phase (i.e., a negative
101 index, see Fan et al., 2023) in the SPG enables the northward expansion of subtropical warm and
102 saline waters, while a strong SPG feeds cold and fresh subpolar waters into the Atlantic inflow.

103

104

105
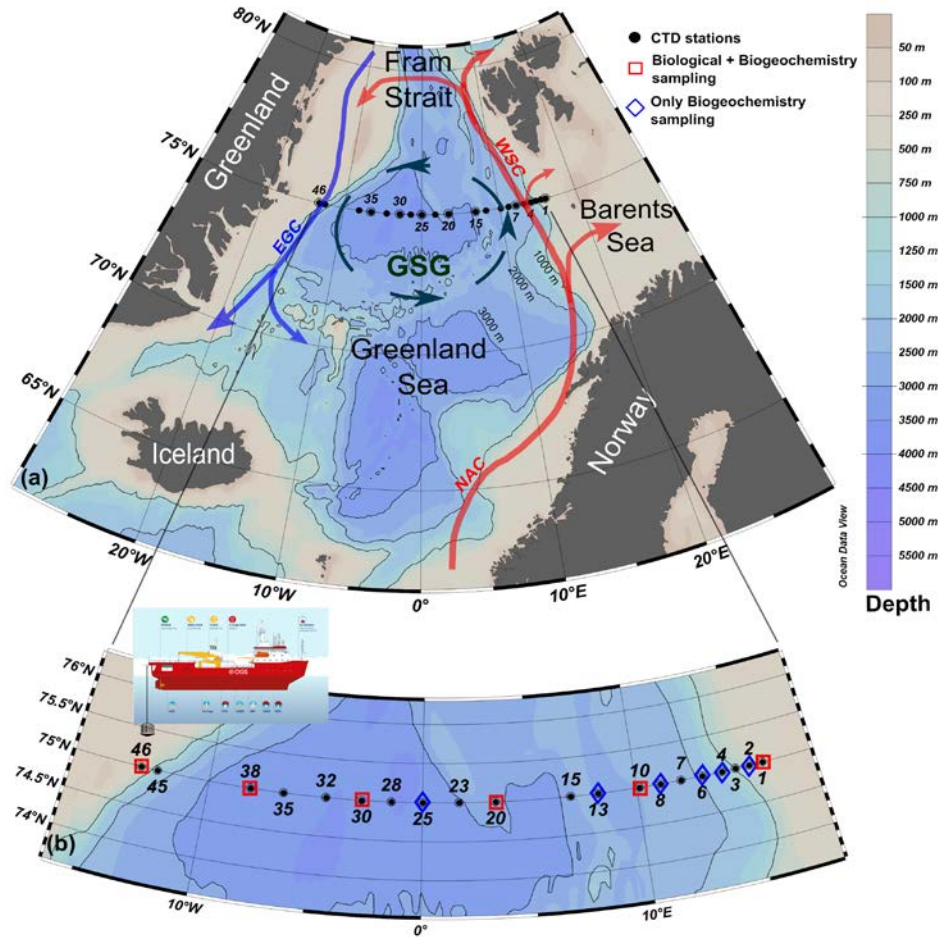
Figure 1 - **(a)** Schematic of the general circulation in the Greenland Sea (**GSG**-Greenland Sea Gyre; **WSC**-West Spitsbergen Current; **EGC**-East Greenland Current; **NAC-** Norwegian Atlantic Current). **(b)** Distribution of hydrological (CTD) stations conducted during the LB21 CASSANDRA cruise (29 August -14 September 2021) with the positions of the physical (black dots), biogeochemical and biological stations (blue and red symbols).

A time lag of 3-5 years is expected for the thermohaline anomalies to propagate in the Nordic seas (Fan et al., 2023) from the sub polar regions. In other words: while the GSG regulates the AW inflow into the Arctic, the SPG modulates the proportion of subtropical and subpolar waters moving at high latitudes. Wind forcing and heat loss combine to drive the full variability of the flow and water mass transformations in the region (Smedsrud et al., 2022).

The anomalous inflow of AW from the Nordic seas and the subpolar regions is referred to a process called Atlantification, which has various direct and indirect effects on the Arctic environment. This process has intensified since the 2000s, leading to, among other effects, increasing anomalies in temperature and salinity in the upper layer, a reduction in sea ice cover, reduced stratification of the upper ocean, increased primary production and a shift of the summer bloom to earlier periods, changes in the phenology, distribution and community composition of zooplankton, and spreading of subarctic species (Polyakov et al., 2017; Ingvaldsen et al., 2021; Csapò et al., 2021). Microbial communities are also affected by the co-occurrence of Atlantification and Arctic amplification, as pointed out by recent observations (Ahme et al., 2023; Priest et al., 2023). Microorganisms are pivotal drivers in all the earth ecosystems, as primary degraders of organic matter and main players in nutrient cycling. They are thus particularly sensitive to the external environmental conditions and

126 as such, play a role of optimal sentinels of global changes and trends (Caruso et al., 2016). Distinct
127 bacterial communities have been reported between Atlantic- and Arctic-derived waters (Carter-
128 Gates et al., 2020), and a direct effect of organic matter dissolution from the sea ice on the microbial
129 diversity has been demonstrated, by documenting the occurrence of diverse bacterial assemblages
130 between sea-ice and seawater (Yergeau et al., 2017). The Greenland Sea, like other Nordic Seas, is
131 a sink for atmospheric CO_2 during the year (Skjelvan et al., 2005). The annual flux of CO_2 absorbed
132 by the sea has been estimated at 53 gC m^{-2} yr^{-1}. Of this amount, about half was attributed to the flux
133 caused by heat loss and the other half to biological production (Anderson et al., 2000). Higher
134 estimates of annual fluxes, ranging from 40 to 85 gC m^{-2} yr^{-1}, were presented by Skjelvan et al.
135 (2005 and reference therein). Total carbon in surface waters varies seasonally because of physical
136 and biological processes that influence the amount of carbon exported to deep waters (von
137 Bodungen et al., 1995; Noji et al., 1999). The mixing of the open ocean contributes to the transport
138 of carbon from the surface to the deep interior. As a result of the increasing CO_2 input from the
139 atmosphere, the pH in the Nordic Seas has decreased by ~0.0028 units per year in the period 1981-
140 2019 (Frasner et al., 2022).

141 Here, we present data and main results obtained in the framework of the CASSANDRA (*advanCing*
142 *knowledge on the present Arctic Ocean by chemical-phySical, biogeochemical and biological*
143 *obServAtioNs to preDict the futuRe ChAnges*) project funded by the Italian Arctic Research
144 Programme (*https://www.programmaricercaartico.it/*). CASSANDRA contributed to the Synoptic
145 Arctic Survey (SAS) by investigating the historical zonal transect at 75°N through the Greenland
146 Sea Gyre during the summer of 2021 (29 August - 14 September). The SAS initiative aims to
147 quantify the current state of the Arctic Ocean and its changes, focusing on water masses,
148 ecosystems, and the carbon cycle (see https://synopticarcticsurvey.w.uib.no/). SAS sees the
149 participation of 11 countries in 25 Arctic cruises.

2   DATA and METHODS

151 The LB21 CASSANDRA cruise (hereinafter, LB21 cruise) was carried out between 29 August 2021
152 (Longyearbyen, Svalbard) and 14 September 2021 (Bergen, Norway) on board the icebreaker Laura
153 Bassi (https://www.ogs.it/en/research-vessel-laura-bassi). All methods used for the CASSANDRA
154 activities were in line with the recommendations of the SAS and Go-Ship programme
155 (https://www.go-ship.org/), the latter including the 75°N transect. This approach was chosen to
156 obtain data that were as comparable as possible to other the SAS programme cruises. During the
157 LB21 cruise, a total of 28 vertical Conductivity-Temperature-Depth (CTD) profiles were conducted
158 at 20 hydrological stations (some stations include repeated casts). Of these, biogeochemical and
159 biological data were also collected at 12 and 6 stations, respectively (see Fig. 1). Unfortunately,
160 some technical problems and 2 days of adverse meteorological conditions in the middle of the cruise
161 prevented the completion of all planned stations. Some of the figures presented here were created
162 with Ocean Data View (Schlitzer, 2024).

2.1 Hydrographic data

164 All hydrographic profiles were recorded with a Seabird SBE911plus, equipped with some additional
165 sensors. CTD measurements provide vertical profiles of temperature (T) and conductivity (C)
166 approaching the seafloor to ~ 5–10 m, depending on sea conditions. Potential temperature (θ),

167 salinity (S), and potential density anomaly (σ_θ, referred to 0 dbar) were calculated from *in situ* data
168 using the MATLAB toolbox TEOS-10 (Gibbs SeaWater Oceanographic Toolbox) including the
169 thermodynamic equations for seawater (http://www.teos-10.org/software.htm). Dissolved Oxygen
170 concentration was measured using an SBE43 sensor. T and S data were quality checked and
171 averaged every 1 dbar, with overall accuracy within ± 0.002 °C for T, ± 0.005 for S and 2% of
172 saturation for oxygen. Fluorescence and turbidity in the water column were measured with optical
173 sensors WET Labs ECO-AFL/FL. Water sampling was carried out using a rosette system equipped
174 with 24 10-liter Niskin bottles.

2.2 Biogeochemistry data

176 The chemistry of seawater was investigated at 12 stations from discrete water samples (Fig. 1) by
177 measuring dissolved oxygen, nutrients (nitrite, nitrate, phosphate, silicate), dissolved and particulate
178 Carbon (DOC and POC), total dissolved nitrogen and phosphorus (TDN and TDP); $\delta^{18}O$ and δD of
179 H_2O; inorganic carbonate system characterization by total alkalinity, pH_T and derived parameters.
180 The dissolved oxygen concentration (DO) was determined by a potentiometric Winkler titration
181 (Oudot et al., 1988; Grasshoff et al., 1999). Samples for inorganic nutrients (nitrite - NO_2, nitrate -
182 NO_3, ammonium - NH_4, phosphate - PO_4 and silicate - $Si(OH)_4$) were collected and analysed as
183 described in Ingrosso et al. (2016a) using a four-channel Continuous Flow Analyzer QuAAtro (Seal
184 Analytical Inc., Mequon, WI, USA) autoanalyzer. Detection limits were 0.01 µmol L^{-1}, 0.02 µmol
185 L^{-1}, 0.03 µmol L^{-1}, 0.01 µmol L^{-1} and 0.01 µmol L^{-1} for NO_2, NO_3, NH_4, PO_4 and $Si(OH)_4$,
186 respectively. DON and DOP were calculated as the difference between dissolved total phosphorus
187 (TDP) and PO_4 and between dissolved total nitrogen (TDN) and dissolved inorganic nitrogen (DIN
188 = $NO_3 + NO_2 + NH_4$), respectively. TDP and TDN were determined as PO_4 and NO_3, respectively,
189 after quantitative conversion to inorganic P and N by persulfate oxidation (Hansen and Koroleff,
190 1999). The accuracy and precision of the analytical procedures are annually checked through the
191 quality assurance program (AQ1) QUASIMEME Laboratory Performance Studies (Wageningen,
192 The Netherlands) and internal quality control samples were used during each analysis. Samples for
193 pH_T analysis were collected and analysed on board as described in Ingrosso et al. (2016b) and Urbini
194 et al. (2020) using a spectrophotometer (Varian Cary 50 UV-visible). The results were expressed
195 on the 'pH total hydrogen ion scale' (pH_T) at 25°C, with a reproducibility of 0.0048, determined by
196 replicates from the same Niskin bottles. To measure total alkalinity (A_T, µmol $kgSW^{-1}$), water
197 samples were collected and analysed as described in Ingrosso et al. (2016a) and Urbini et al. (2020)
198 using the seawater certified reference materials (CRMs) for TCO_2 and A_T supplied by Prof. A.G.
199 Dickson, Scripps Institute of Oceanography, USA (Batch number #185) to calibrate HCl for
200 analyses. A_T precision and the accuracy were less than ± 2.0 µmol kg^{-1}, assessed by analysing
201 CRMs. All other carbonate system parameters, including pH_T at *in situ* temperature, seawater partial
202 pressure of CO_2 (pCO_2), TCO_2, and aragonite saturation state (Ω_{ar}) were calculated using the
203 CO2Sys program as described in Urbini et al. (2020). The estimated uncertainties were: ±0.005 for
204 pH_T at in situ temperature, ±7.8 µatm for pCO_2, ±5.6 µmol kg^{-1} for TCO_2 and ±0.12 for aragonite
205 saturation state. Samples for stable isotopic composition of dissolved inorganic carbon ($\delta^{13}C$-DIC)
206 were collected in 12-mL Exetainer® (Labco Limited, Ceredigion, UK) evacuated glass tubes,
207 containing 2 µL of saturated $HgCl_2$. Samples were stored at 4 °C in the dark until analysis was
208 performed as described in Relitti et al. (2020). To determine the optimal extraction procedure for

209   water samples, two standard Na_2CO_3 solutions were prepared with a known ^{13}C value of $-10.8 \pm$
210   0.1 ‰ (k=1) and -4.2 ± 0.1 ‰ (k=1), respectively. The stable isotopic composition of dissolved
211   inorganic carbon is given conventionally in δ-notation in per mil deviation (‰) from the Vienna
212   Peed Dee belemnite (VPDB) standard.

213   For POC concentrations filters were freeze-dried and subsampled by punching 18% of the 45 mm
214   filter area and fitted into silver capsules/boats. The subsamples were treated with 1M HCl to remove
215   inorganic carbon and then placed into an oven at 60 °C until dry. Afterwards, the samples were
216   wrapped in tin capsules/boats to aid combustion during analysis. The samples were analyzed with
217   a Thermo Fisher elemental analyzer (FLASH 2000 CHNS = O) coupled with a Thermo Finnigan
218   DeltaC isotope ratio mass spectrometer (IRMS). At least two replicates were analysed for each
219   sample. Spatial variability was within ± 2.5 % on the filter.

220   Water samples for DOC analyses were filtered aboard, immediately after collection, through
221   precombusted (4 h at 480 °C) Whatman GF/F glass fibre filters (0.7 μm nominal pore size).
222   Filtration was performed by using a disposable polycarbonate syringe and a polypropylene 25 mm
223   filter holder (Nuclepore), to prevent atmospheric contamination. Filtered samples were stored in 25
224   mL high density polyethylene (HDPE) bottles (previously treated with HNO_3 1.2 M at 50 °C for 1
225   h) which were quickly frozen in an aluminium block at -20 °C. In the laboratory, filtered samples
226   were thawed, acidified to pH = 2 with ultrapure HCl and purged with N_2 for about 10 min to remove
227   inorganic carbon, as outlined in Pettine et al. (2001). Dissolved organic carbon (DOC) was assayed
228   by high temperature catalytic oxidation (HTCO) using a Shimadzu TOC-L series analyser.

229   Samples for stable isotope ratio measurements in seawater were collected in 5 mL amber glass
230   bottles. The bottles were filled to avoid the presence of air, immediately sealed and stored at a
231   temperature of 4 °C until the analyses. Analyses were performed by means of a Thermo DeltaV-
232   Advantage mass spectrometer equipped with a gas-bench. For the analysis, a quantity of 200 μL of
233   water sample was used in a glass vial firmly closed with a membrane cap. The samples were flushed
234   with a gas mixture of 2% H in helium with a purity of 99.998 and analysed to determine δD.
235   Immediately after the δD analyses, the same samples were flushed with a gas mixture of 0.4% CO_2
236   in helium with a purity of 99.998 and analysed to determine $δ^{18}O$ after 20 hours of equilibration.
237   All samples were measured at least in triplicate and the isotopic data are the mean of consistent
238   results. The standard deviation of our results is always 0.50‰ and 0.06‰ or better for δD and $δ^{18}O$,
239   respectively. The SMOW2 and SLAP2 isotopic standards were used as a reference together with a
240   'home-made' standard. The home-made standard is analysed every 3 measurements (3 replicates of
241   a single sample) to assess the stability of the measurements. The isotopic composition is expressed
242   as:

243    $$δX = [(R_s-R_r)/R_r] \times 1000$$

244   where δX represents δD or $δ^{18}O$, R=D/H or $^{18}O/^{16}O$ in the sample (s) and in the reference (r),
245   respectively.

2.3 Phytoplankton data

2.3.1 Total and size-fractionated chlorophyll a (chl-a)

Chlorophyll *a* (chl-*a*) and phaeopigment (phaeo) concentration were measured fluorometrically. Samples were filtered on Whatman GF/F glass-fiber and polycarbonate membranes (of 2.0 and 10.0 µm) to separate three size fractions: micro-phytoplankton (> 10 µm), nano-phytoplankton (10–2.0 µm) and pico-phytoplankton (2.0–0.45 µm) as reported in Decembrini et al. (2021).

2.3.2 Utermöhl phytoplankton

For the determination of Utermöhl phytoplankton (i.e., all species/taxa detectable by light microscopy, thus excluding prokaryotic phytoplankton and the majority of picoeukaryotes < 1 µm), 500-mL water samples were collected in opaque polyethylene bottles and immediately fixed with pre-filtered and neutralised formaldehyde (1.6% final concentration) (Throndsen, 1978). Inverted microscopes equipped with phase contrast (Zeiss Axiovert 200M and Leica DMi8) were used for the taxonomic identification analysing a variable volume of sample (10-50 mL), according to the Utermöhl method (Zingone et al., 2010). Counting was performed along transects across the microscope chambers at a magnification of 400x for small (5-20 µm) or very abundant species and observing half of the sedimentation chamber at a magnification of 200x for less abundant microphytoplankton (> 20 µm). The abundance was expressed as the number of cells per liter (cells L^{-1}). The minimum value of the counted cells was 200 cells per sample for a confidence limit of 14% (Andersen & Throndsen, 2004).

2.4 Zooplankton data

2.4.1 Microzooplankton

Microzooplankton (MZP) samples were collected in six stations at different depths depending on water column vertical profiles (Fig. 1). For MZP analyses, 10 L of seawater were reverse filtered through a 10 µm mesh to reduce the volume to 250 mL and immediately fixed with buffered formaldehyde (1.6% final concentration). Subsamples (50 mL) were then examined in a settling chamber using an inverted microscope (magnification 200x) (Leitz Labovert, Leica DMI 300B), following the Utermöhl method (1958). The entire surface of the chamber was examined. Among the MZP community, five main groups were considered: heterotrophic dinoflagellates, aloricate ciliates, tintinnids, micrometazoans and other rare protozoans. Tintinnids empty loricae were not differentiated from filled loricae because the tintinnid protoplasts are attached to the lorica by fragile strands that can easily detach during the collection and fixing of the samples. For each taxon, the biomass was estimated by measuring the linear dimensions of each organism with an eyepiece scale and relating the shapes to standard geometric figures. Cell volumes were converted into carbon values using the appropriate conversion factors, as follows: aloricate ciliates, pg C $cell^{-1}$ as μm^3 x 0.14 (Putt and Stoecker, 1989); tintinnids, pg C $cell^{-1}$ as μm^3 x 0.053 + 444.5 (Verity and Langdon, 1984); athecate heterotrophic dinoflagellates, pg C $cell^{-1}$ as μm^3 x 0.11 (Edler, 1979); thecate heterotrophic dinoflagellates, pg C $cell^{-1}$ as μm^3 x 0.13 (Edler, 1979); other protozoans, pg C $cell^{-1}$ as μm^3 x 0.08 (Beers and Stewart, 1970).

2.4.2 Mesozooplankton

Three hauls were conducted at six stations (Fig. 1): one horizontally at the surface with the Manta net (333 µm, 0.098 m^2 net opening) and 2 vertically (from 100 m depth to the surface) with the WP2 net. A Hydrobios flowmeter mounted in the net opening was used to measure the volume of seawater filtered through each net. Immediately after the catch, samples were treated to estimate biomass, taxa composition and abundance of the zooplanktonic community. Samples collected with the Manta net were split by using the Huntsman beaker technique (van Guelpen et al., 1982) and treated as follows: half of the sample was fractionated by passing it through a series of steel sieves with decreasing mesh size (> 2 mm; 2-1 mm; 1-0.5 mm; 0.5-0.2 mm) and immediately frozen at -20°C for biomass analysis, ¼ was fixed and preserved in a seawater-buffered formaldehyde solution (4% final concentration) for later determination of taxa composition and abundance and ¼ was fixed in 96% ethanol for molecular analysis (data not shown in this manuscript). Samples collected with the WP2 net were treated as follows: one sample was entirely fractionated and frozen at -20°C for biomass analysis using the same procedure as the Manta net samples, and one sample was split in half and fixed in seawater-buffered formaldehyde solution (4% final concentration) and 96% ethanol, respectively. In the laboratory, to estimate biomass (dry mass), each size fraction was resuspended in a small volume of filtered seawater and dewatered by vacuum filtration on pre-dried and weighed GF/C filters (47 mm diameter) after being briefly rinsed with distilled water to remove the salts of the seawater (Postel et al., 2000). Each filter was then placed in a small plastic Petri dish and dried in an oven at 60 °C for 24 hours or longer until completely dry and weighed on an electronic microbalance. The fixed samples were concentrated to remove the formaldehyde, and the organisms were suspended in filtered seawater and carefully passed through the same set of sieves used for the biomass. Depending on the abundance, the organisms present in the subsamples or in the entire fractionated sample were counted and identified (Copepoda, Chetognata, Mollusca, and others) under stereo-microscopes (Leica 165C :120x; Leica 205C: 160x).

2.5 Microbiological data

2.5.1 Prokaryotic biomass, viable and dead cells, respiring cells

The microbial components were investigated by using different approaches. The detailed methodological procedures for assessing prokaryotic cell abundances, biomass and morphometric features are reported by La Ferla et al. (2012). The viability of prokaryotic cells quantified by the Live/Dead Bac Light Bacterial Viability Kit™ and the number of respiring cells quantified by the Bac Light Redox Sensor CTC Vitality Kit™ were estimated as reported by Azzaro et al. (2022).

2.5.2 Physiological profiles of microbial community

Physiological profiles were determined by the Biolog EcoPlate™ microplate assay. The metabolic potentials of bacterial assemblages were quantified as the optical density (OD) values of the formazan produced by oxidation of the 31 carbon sources included in the Biolog Ecoplates. The absorbance was recorded at 590 nm excitation wavelengths using a compact plate reader Byonoy Absorbance 9 and spectrophotometrically measured according to Azzaro et al. (2022) and references therein.

2.5.3 Microbial activities involved in organic matter decomposition and mineralization (enzymatic and respiratory activity rates)

The potential decomposition rates of organic polymers (proteins, polysaccharides and organic phosphates), mediated by the microbial enzymes leucine aminopeptidase (LAP), beta glucosidase (GLU) and alkaline phosphatase (AP) respectively, were estimated by incubation with fluorogenic substrates derived from methylcoumarin (MCA) and methylumbelliferone (MUF), as reported by Hoppe (1993), adapted by Caruso et al. (2020). Fluorescence readings were converted into enzymatic activity rates and expressed as the maximum rate (Vmax) of hydrolysis of the substrates, in nM h^{-1}.

2.5.4 Respiratory activity

The respiration rates were measured by the Electron Transport System activity (ETS) assay. This method is based on the conversion of tetrazolium salt into formazan. The detailed methodological procedures were reported by Azzaro et al. (2006, 2021) and references therein.

3   RESULTS

The LB21 cruise (see Fig. 1) was conducted in early September, when the seasonal minimum of sea ice extent is recorded in the Arctic and sub-Arctic regions (Fig. 2). The ice extent in the Fram Strait fluctuates from year to year. In the long term, the lowest extent in September was recorded exactly in 2021, the highest in 1987. After 2021, a recovery of the summer seasonal sea ice extent was observed. For winter, the lowest extent was observed in 2006, the highest in 1986. Our cruise therefore took place during the period of the lowest summer sea ice extent measured to date.

343
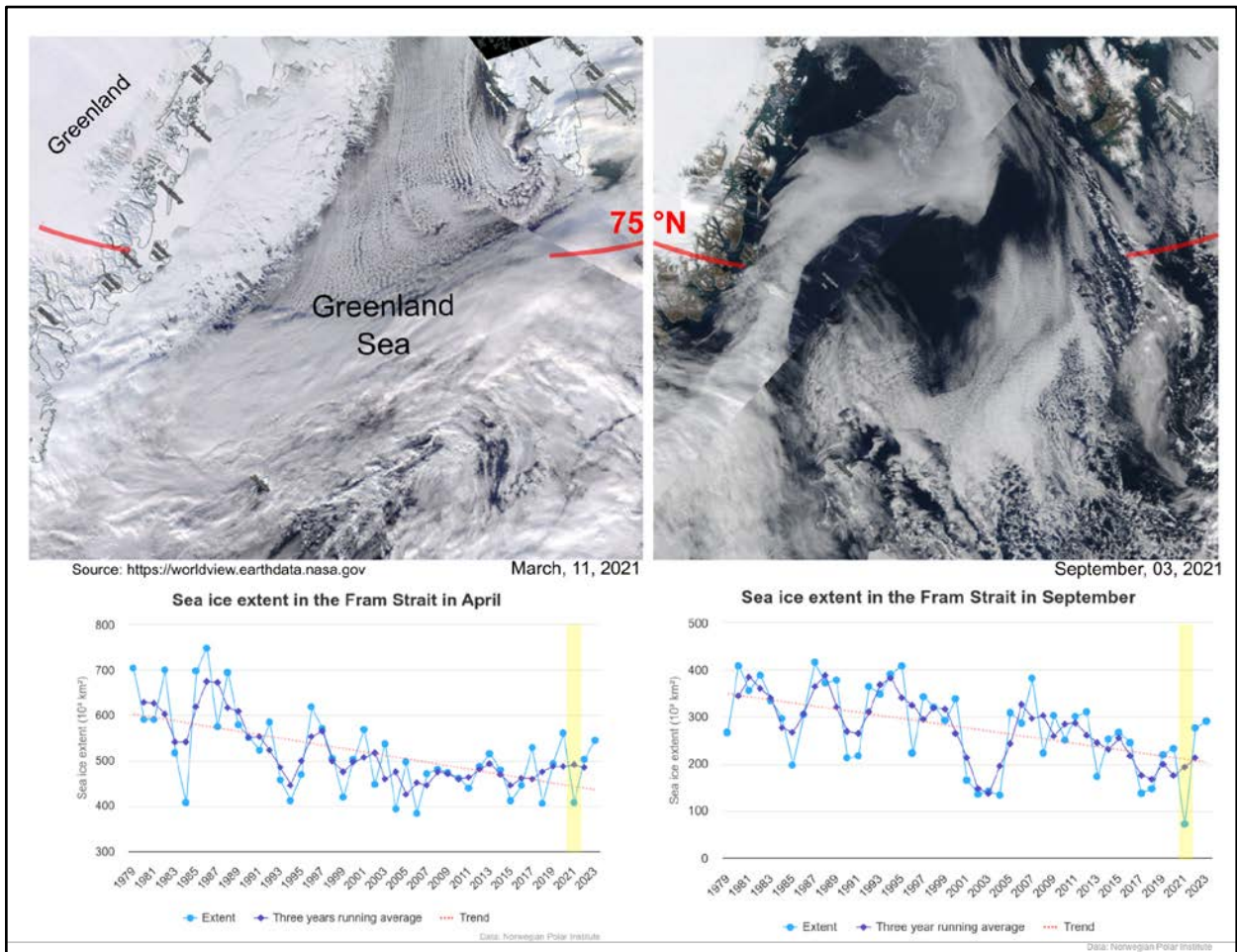
Figure 2 - **Upper panels**: satellite images of the Greenland Sea and the Fram Strait in March and September 2021 (MODIS Corrected Reflectance Imagery, source NASA). **Bottom panels**: April and September mark the annual maximum and minimum sea ice extension in the Fram Strait (source: Norwegian Polar Institute, 2024, Environmental monitoring of Svalbard and Jan Mayen (MOSJ). URL: https://mosj.no/en/indikator/climate/ocean/sea-ice-extent-in-the-barents-sea-and-fram-strait/). The yellow vertical bar indicates the year 2021.

3.1 Physical Oceanography: thermohaline properties distribution

We grouped our data according to the definition of main water masses from Rudels et al. (1999) and Wang et al. (2021) and adjusted them to include most of our data. Due to some data gaps, it was not possible to define all relevant water masses in this area more precisely. Along the zonal transect at 75 °N, the ocean temperature shows a very pronounced horizontal gradient, with typical values of AW ($\theta > 3.0$ °C, S > 35) in the uppermost 500 m of the water column on the eastern side (Fig. 3). At the surface, the AW has temperatures between 4.5 °C and 9.0 °C (Fig. 4). The AW extends to the west and gradually becomes shallower, so that from station 20 to station 35 it only occupies the uppermost 50-80 metres. In contrast, the surface layer on the western side, from station 38 to 46, has a thin (about 40-80 m) layer of Polar Water (PW) with temperature and salinity values that are typical of sea ice meltwater ($\theta < 0$ °C, S $\leqq$ 33). The intermediate zone between 100 m and 500 m is largely occupied by mixed water and we refer to it as the transition layer. The deep layer below 500 m depth is occupied by Greenland Sea Arctic Intermediate Water (GSAIW, $-0.9 < \theta < 0$ °C, S ~ 34.9), Greenland Sea Deep Water (GSDW, $\theta < -1$ °C, S < 34.9) in the central and westernmost part, respectively, and Norwegian Sea Deep Water (NSDW, $\theta \sim -1.0$ °C, S ~ 34.9) in

the easternmost part of the section. We find that the deep layer below 500 m has homogeneous thermohaline properties, with a slightly pronounced difference at the easternmost edge where the NSDW flows northwards. Isotherm at 0 °C and the overall distribution of isopycnals (Fig. 3 a, c) show a classic dome shape with an upwelling in the central part caused by the effect of the GSG, which tends to lift the intermediate water towards the surface due to its cyclonic (i.e., anticlockwise) sense of rotation. In addition, we are certain that the strong horizontal shear and local meteorological conditions can induce the formation of several mesoscale structures (i.e., eddies, hardly shown by our spatial resolution ranging from about 20 km (along the sides) to 40-60 km (in the centre of the transect). They can change the internal distribution and even trap nutrients and other chemical-biological properties. The dissolved oxygen values show a higher oxygen enrichment (> 350 µmol kg^{-1}) in the intermediate layer between stations 15 and 38 (Fig. 3d), while the maximum values are found in the upper layer near the Greenland coasts, where the PW flows southwards. In contrast, lower oxygen values (< 300 µmol kg^{-1}) are found below 1500 m depth and in the easternmost part of the section where AW and NSDW occur (Fig. 3d). Turbidity is higher at the surface and along the continental slopes, both on the eastern and western sides, while the fluorescence maximum is at a depth of about 25-30 m and higher values are found in the easternmost part of the section (Fig. 3e, f). Overall, θ spans from 1.5 °C to almost 9 °C, while S spans from 30 (melting waters) to 35 (AW, Fig. 4).
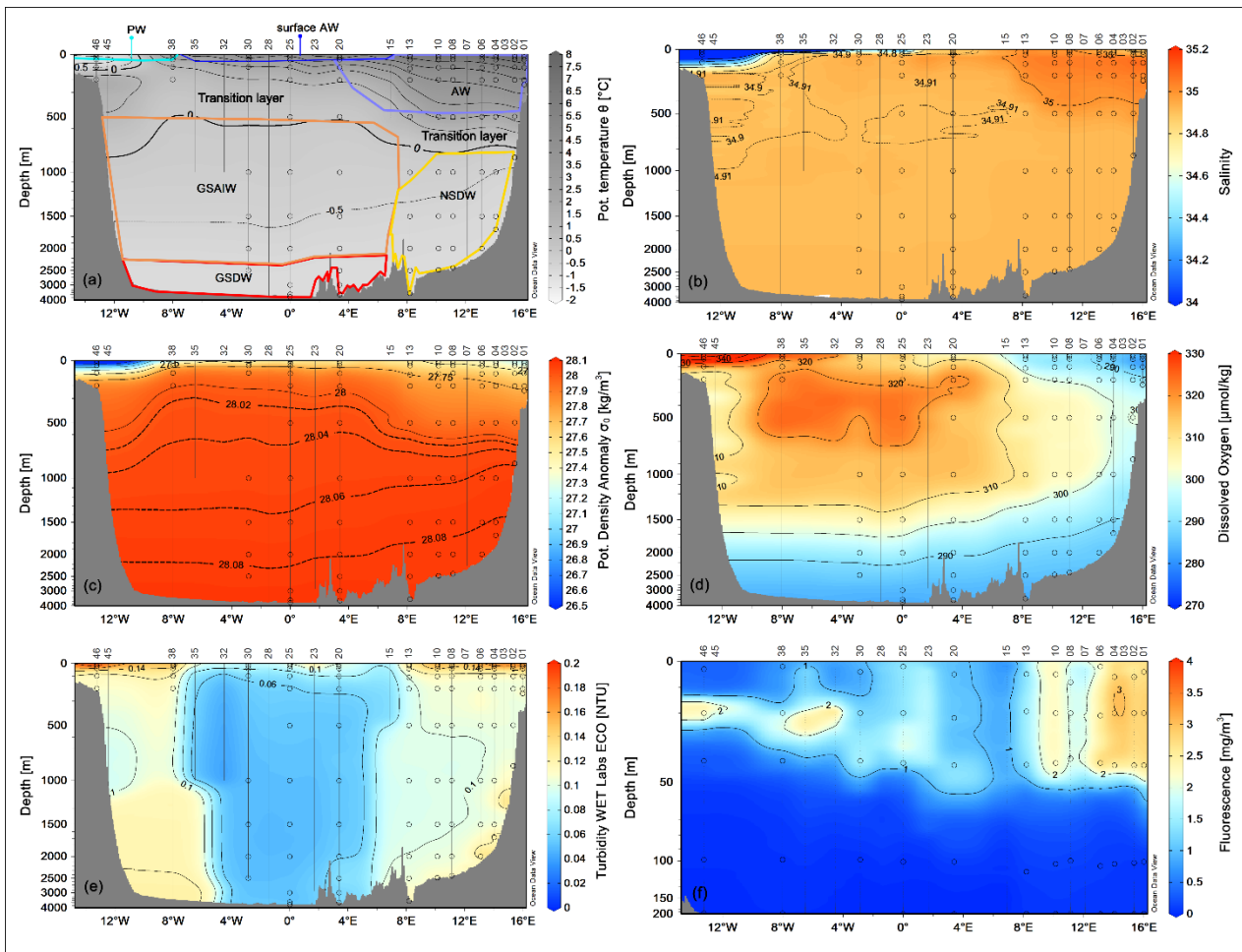
Figure 3 - Vertical distribution of (a) potential temperature (°C), (b) salinity, (c) potential density anomaly (kg m^{-3}), (d) dissolved oxygen (µmol kg^{-1}), (e) turbidity (NTU), and fluorescence (mg m^{-3}) along the zonal transect at 75° N in September 2021. The empty dots indicate the sampling points of the Niskin bottles. Panel a show also the distribution of

principal water masses according to their core values [**AW** - Atlantic Water; **GSAIW** - Greenland Sea Arctic Intermediate water; **NSDW** - Norwegian Sea Deep Water; **GSDW** - Greenland Sea Deep Water; **PW** - Polar Water or Melting Water]. Depths on y-axis are non-linear.
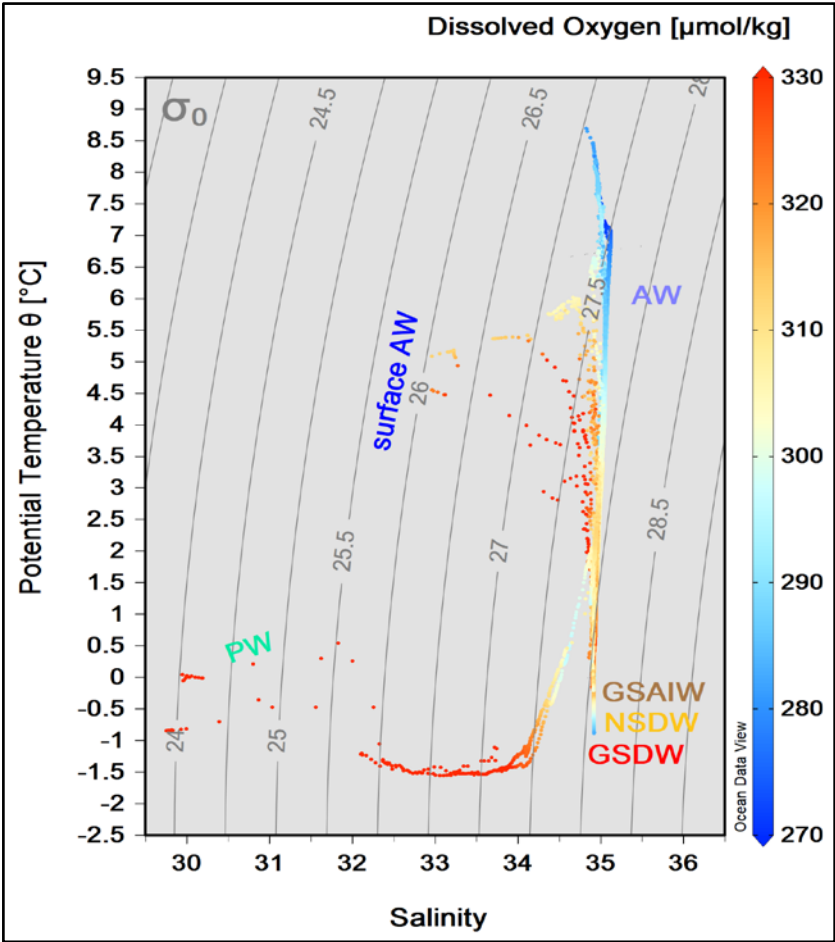
Figure 4 - θ/S diagram from the CTD data collected along the 75 °N section, during the LB21 cruise in September 2021. The colorbar on the right-hand side refers to the values for dissolved oxygen concentration (µmol kg^{-1}). [For water masses acronyms see caption of figure 3].

3.2 Biogeochemistry

Along the entire transect, except for the two edges, the seasonal warming in summer had created a well-stratified upper layer about 30-50 metres deep. At the surface, the central Greenland Sea appears to be almost nutrient poor (Fig. 5). The western side of the transect is characterised by higher concentrations of phosphate and silicate, good indicators of the upper halocline of Arctic surface water along the Greenland slope, whereas nitrate concentrations are very low. At depth, NSDW and GSDW (see Fig. 3, 5) were enriched with silicate.
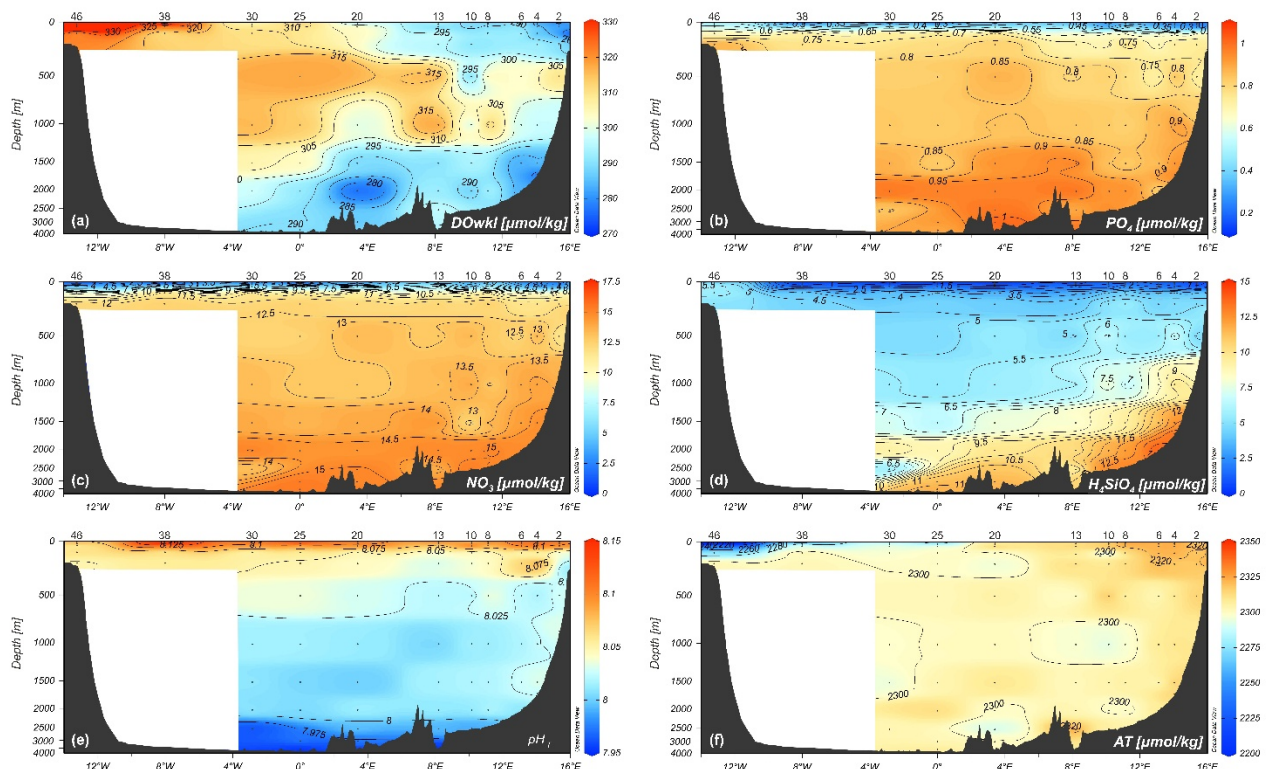
Figure 5 - Vertical distribution of (a) dissolved oxygen concentration (µmol/kg), (b, c, d) nutrients concentration (µmol/kg), (e) pH$_T$, and (f) Total Alkalinity (µmol/kg) along the zonal transect at 75° N during the LB21 cruise in September 2021. Data are obtained from the laboratory analyses on water samples. Depths on y-axis are non-linear.

A marked vertical gradient is found along the entire transect with higher pH$_T$ values (up to 8.227, Fig. 5e) in the photic layer (< 100 m depth) decreasing with increasing depth and reaching the lowest values (7.946-7.997) in the deep layer of the Greenland Sea, presumably due to the degradation of settling organic matter. High total alkalinity values (Fig. 5f) are found on the easternmost side where the AW and NSDW flow northwards. The highest values (A$_T$ up to 2320-2348 µmol kg^{-1}) are found in the higher salinity AW and particularly in the photic layer also due to the contribution of photosynthetic activity. The lowest values are instead associated with fresh Polar Water found at the surface on the westernmost part of the section.

At the surface layer, a high variability in the organic matter pool (POC and DOC) is observed (Fig. 6); a decreasing trend down to 1000 m depth and an increase towards greater depths characterise the vertical profiles of DOC. POC concentrations range from 11.2 µg C L^{-1} (St 30, at 2002 m depth; 0.93 µM C) to 160 µg C L^{-1} (St 46, at 198 m depth; 13.3 µM C). A greater variability with depth is observed (coefficient of variation higher than 65). The highest values are generally found at the surface and within the depth interval of 20–40 m. The highest (mean) concentration is measured at station 46 (80.5 ± 53.4 µg C L^{-1}), while slightly lower (mean) values are found at stations 1, 30 and 38 (67.2 ± 46.8; 41.0 ± 23.1 and 60.0 ± 15.3 µg C L^{-1}, respectively), and the lowest values are found at stations 10 and 20 (34.1 ± 31.0 and 28.2 ± 20.5 µg C L^{-1}, respectively). DOC shows classic vertical profiles, with the highest concentrations (1.22 mg C L^{-1}; 101.7 µM C) at station 30 (20 m depth) and a decrease to a minimum of 0.5 mg C L^{-1} (41.7 µM C) at station 10 (499 m depth). Between 200 and 1000 m depth, the values remain low (mean 0.83 ± 0.22 mg C L^{-1}; 69.2 ± 18.3 µM C), while a slight increase was observed in the bottom water, particularly at stations 20 and 10 (Fig. 6).
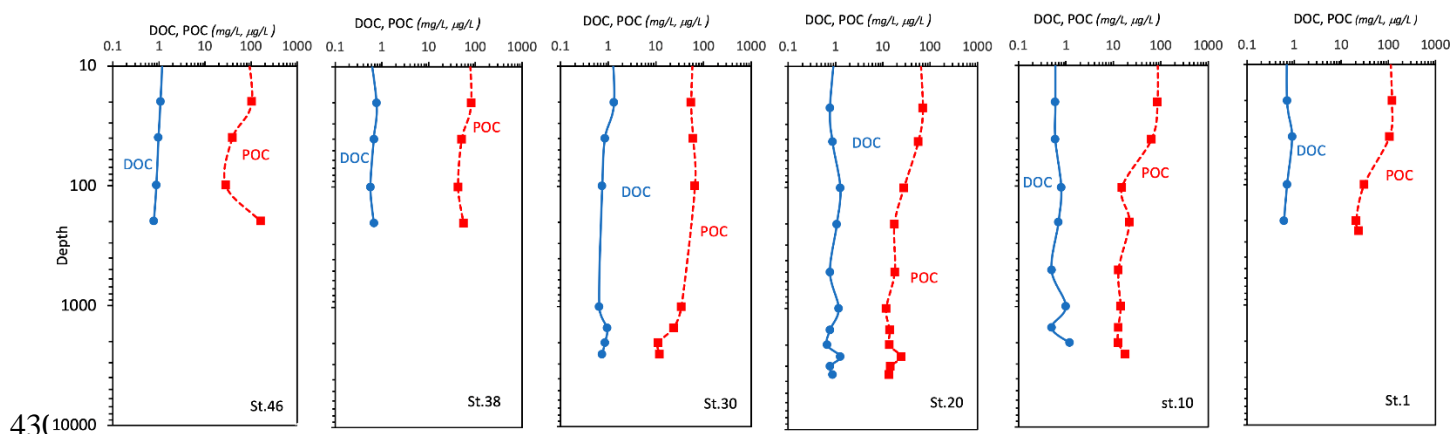
Figure 6 - Vertical profiles of Dissolved Organic Carbon (DOC, mg L^{-1}) and Particulate Organic Carbon (POC, µg L^{-1}) concentrations; Data are represented in natural log (*ln*) scale.

The isotope values in the total of 96 analysed samples range from -0.43 to 0.8‰ for δ^{18}O and from -2.51 to 5.36‰ for δD. Along the transect, a gradient from west to east can be seen in the surface waters, with lower values for δ^{18}O and δD on the westernmost side (Fig. 7). The lowest values at the surface in the westernmost part of the section could be related to fresh PW, while the higher values in the easternmost part could be related to northward flowing AW. At depths between 500 and 1000 m, isotope values drop to a relative minimum, while maxima occur near the bottom at stations 20 and 25, where GSDW is identified. In addition, a minimum is observed at depth at stations 8 and 10, in an area occupied by NSDW.
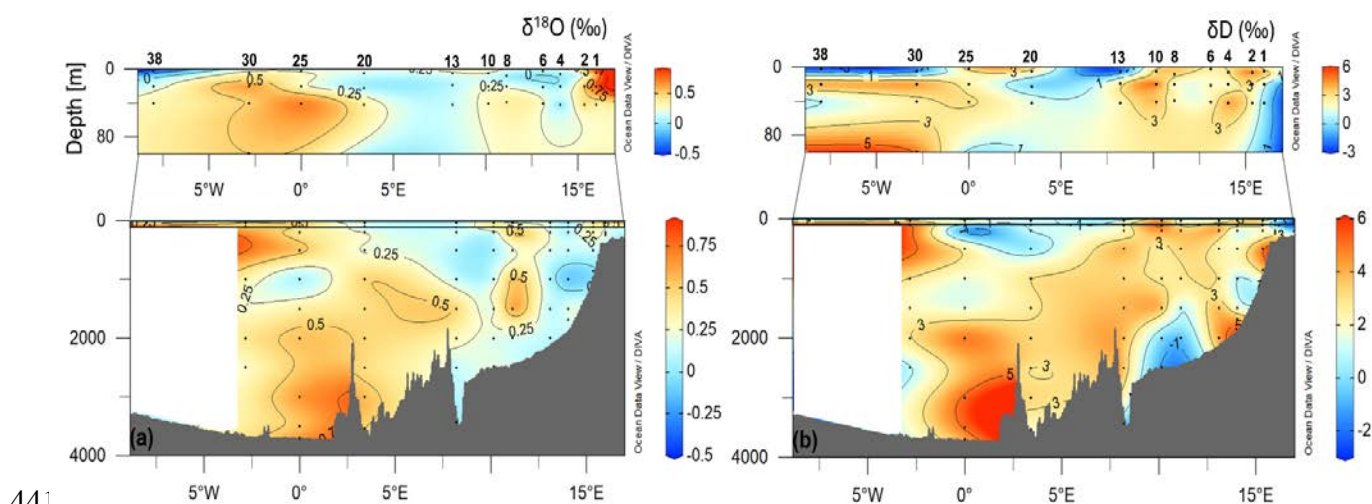
Figure 7 - Vertical distribution of δ^{18}O (a) and δD (b) along the zonal transect at 75° N during the LB21 cruise in September 2021.

3.3 Phytoplankton

3.3.1 Total and size-fractionated chlorophyll *a* (chl-*a*)

Integrated total chl-*a* in the euphotic layer (0-100 m) averages 55.4 mg m^{-2}, while the highest concentrations (73.1 mg m^{-2}) are found at stations located at the ends of the transect (65.3 mg m^{-2}) close to the continental shelf (Fig. 8). The concentration of chl-*a* at different depths ranges between 0.20 mg m^{-3} (St.1, 100 m) and 2.90 mg m^{-3} (St.1, 20 m) with an average value of 0.63 ± 0.64 mg m^{-}

[3]. Degraded pigments (phaeo) are around 40 % with respect to chl-*a*. The size spectrum of the phytoplankton community biomass along the water column, shows different percentage contributions to the total with 65% for the nano-phytoplankton, 21% for the micro-fraction and 14% for the pico-phytoplankton (Fig. 8). Exception to this composition is observed in the westernmost station (st. 46) where the micro-fraction dominates, replacing the nano-phytoplankton.
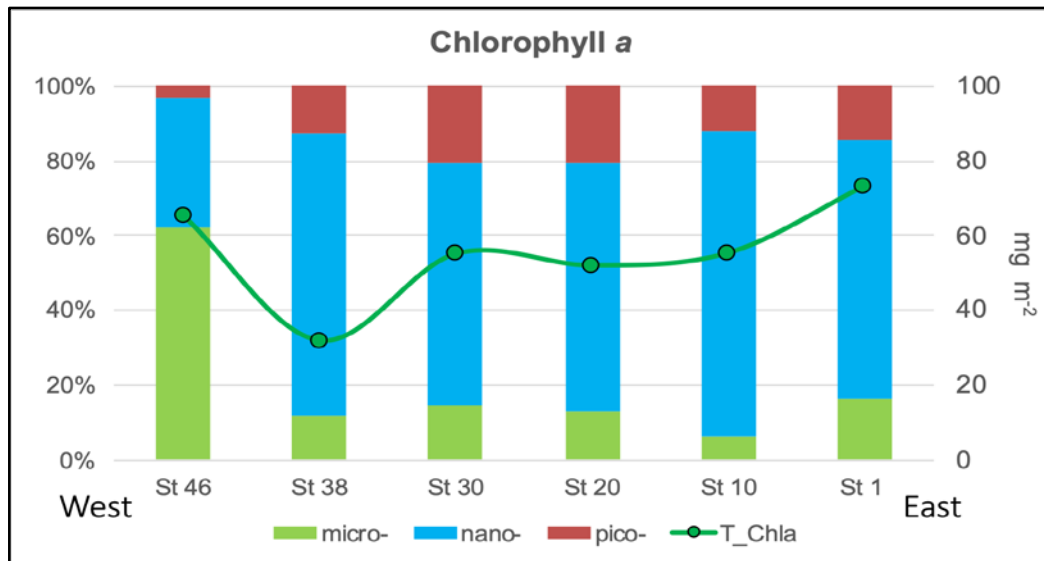
Figure 8 - Integrated total chl-*a* concentration (0-100 m depth) at the stations along the 75°N zonal transect (green line) with the percentage of contribution of micro- nano- and pico-phytoplankton size-fractions (histogram).

3.3.2 Phytoplankton composition and abundances

The phytoplankton analyses do not reveal a clear pattern along the transect, although some differences in abundance and composition were observed. The integrated abundances of phytoplankton, ranging from 7.00 (st. 30) to 23.48 x 10^4 cells L^{-1} (st. 20), are higher at the easternmost stations than at the westernmost ones (on average 19.33 x 10^4 cells L^{-1} at stations 1, 10, 20 and 9.44 x 10^4 cells L^{-1} at stations 30, 38, 46, see Fig. 9). This is mainly due to a more even vertical distribution of abundance at the eastern stations. In contrast, the westernmost stations have even higher phytoplankton abundances, but limited to subsurface maxima, like 50.40 x 10^4 cells L^{-1} at 38 m at station 20, while abundances in the rest of the water column are very low. The phytoplankton community along the transect is characterised by the dominance of the flagellate group (70% of the total phytoplankton), mainly represented by small (< 10 μm) forms with uncertain taxonomic identification (on average, 61%). Diatoms (on average, 9% of the total phytoplankton) are present in very low abundances in the easternmost and central stations (on average, 0.43 x 10^4 cells L^{-1} at stations 1, 10, 20, 30), while higher values were recorded in the two westernmost stations 38 and 46 (on average, 3.24 x 10^4 cells L^{-1}). Finally, dinoflagellates accounted for an average of 21% of the total phytoplankton, with higher abundances occurring in the easternmost stations than in the westernmost stations (3.32 x 10^4 cells L^{-1} and 1.42 x 10^4 cells L^{-1}, respectively).

476
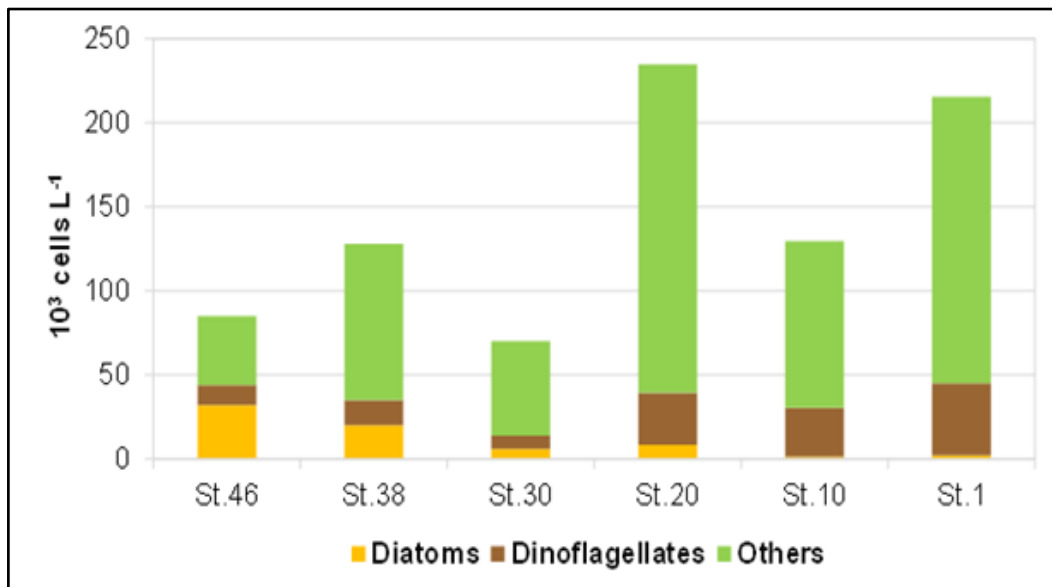
Figure 9 - Integrated contribution of the main phytoplankton groups (diatoms, dinoflagellates, and others) to
phytoplankton abundance at sampled stations along the 75°N transect.

3.4 Zooplankton

3.4.1 Microzooplankton abundance and biomass

The MZP abundance in the study area varies between 721.5 ind. L^{-1} (St. 38, at 0 m) and 6.25 ind. L^{-1} (St. 20, at 3500 m). The carbon content shows higher values at the surface with a maximum value of 1.7 µgC L^{-1} (St. 38, 0 m) and a minimum of 0.01 µgC L^{-1} at 2520 m depth (St. 10). The vertical distribution of organisms, based on their abundance along the water column, shows higher abundances in the first 200 m, compared to the zone > 200 m. In particular, the integrated abundance of MZP in the upper layer reaches its maximum at St. 38, mainly due to the higher presence of tintinnids, while the lowest values are found at St. 20, in the centre of the transect (Fig. 10). The highest carbon content is recorded at St. 10, which is due to the high abundance of other protists and micrometazoans (Fig. 10). Tintinnids are the most abundant taxa in the study area, followed by heterotrophic dinoflagellates and aloricate ciliates (Fig. 10).

491
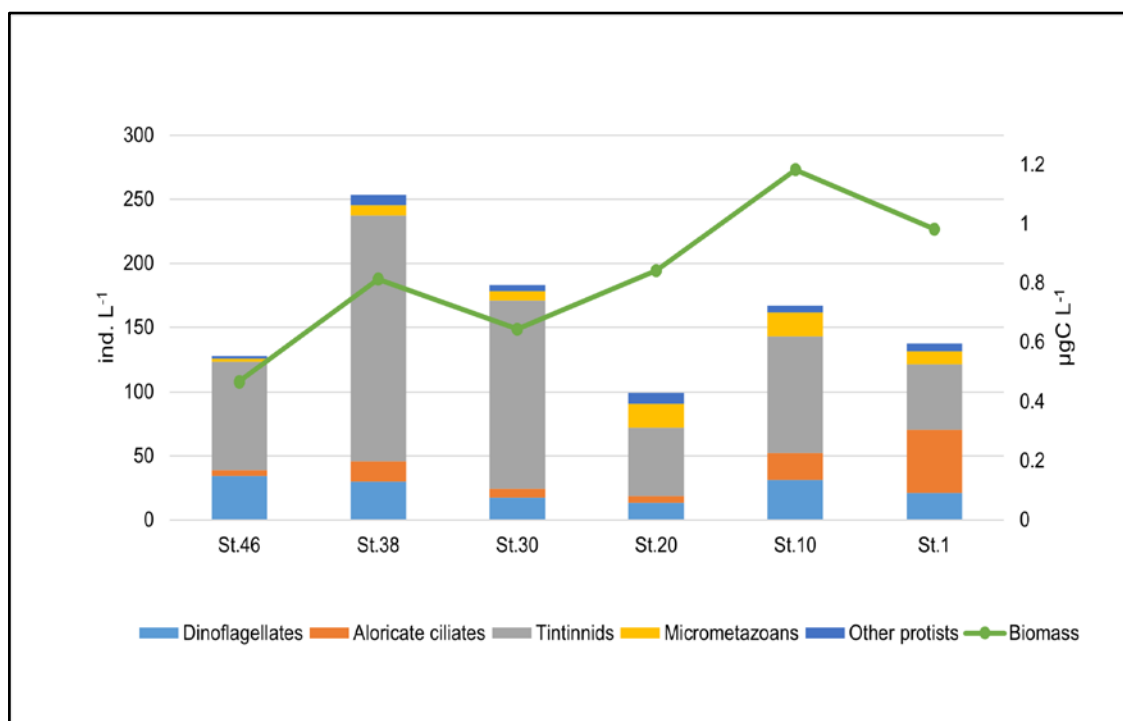
Figure 10 - Integrated values of abundance (ind. L^{-1}) and biomass (μgC L^{-1}) of microzooplankton in the upper layer (< 200 m depth).

3.4.2 Mesozooplankton biomass and abundance

Biomass and abundance of mesozooplankton have the same distribution along the transect both at the surface (ca. 20 cm depth, Fig. 11a) and in the upper layer (0-100 m depth, Fig. 11b), with the highest values found in the central part of the transect (St. 20). Nevertheless, the surface samples are richer in organisms than those collected in the water column (mean abundance: Manta net: 1257 ± 1110 ind. m^{-3}; WP2 net: 492 ± 387 ind. m^{-3}), which also corresponds to a higher biomass (mean biomass: Manta net: 41 ± 32 mgDM m^{-3}; WP2 net: 10 ± 7 mgDM m^{-3}). Overall, organisms 1-2 mm in size account for 61 % of the mesozooplanktonic biomass in the surface waters and are the most abundant at almost all stations (Fig. 11a), while in the samples collected with the WP2 net, the biomass fractions consisting of organisms 1-2 mm and > 2 mm in size were the most abundant, accounting for 35 and 38 % of the total biomass, respectively (Fig. 11b). Copepods are the most abundant taxon both at the surface and in the upper layer (97 % and 94 % of the total mesozooplankton abundance, respectively), mainly represented by the genus *Calanus*. Chaetognaths, although much less abundant than copepods, are found along the entire transect both at the surface and in the upper layer, being most numerous at stations 10, 20, and 30. Molluscs are almost absent in the surface water and are mainly found in the water column at the eastern stations of the transect (St. 1 and St.10).
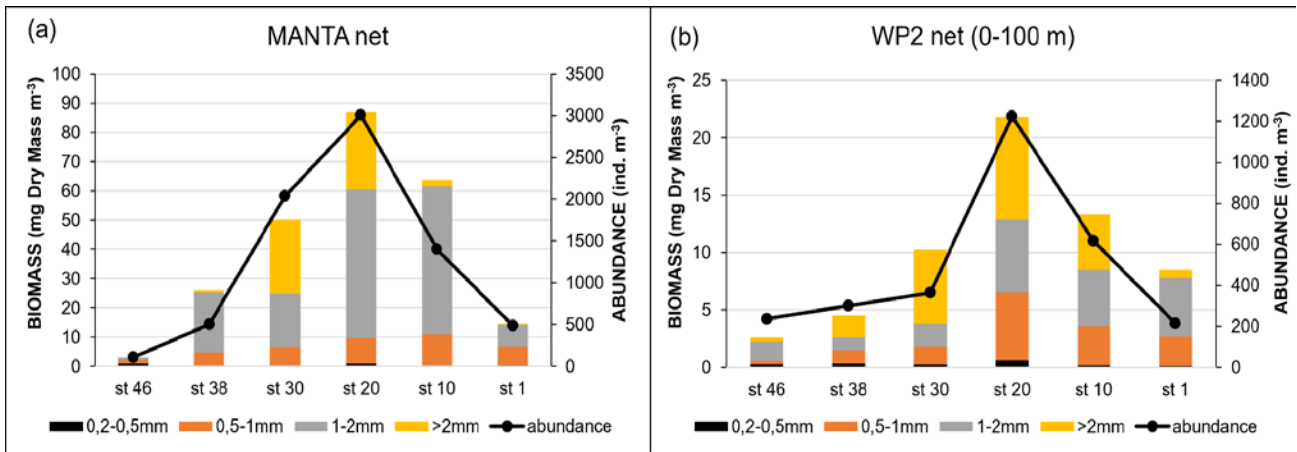
Figure 11 - Biomass and abundance of mesozooplankton: (a) Manta net sampling at surface and (b) WP2 net sampling in the 0-100 m layer.

3.5 Microbial compartment: abundance, biomass, and activities

The abundance of prokaryotes is high in the photic (0-100 m depth) layer (range: 5.57 to 11.3 x 10^5 cells m^{-3}) and decreases with depth. The highest values are measured at stations 20 and 1. From 100 to 1000 m depth, the abundance ranges from 1.75 to 3.21 x 10^5 cells m^{-3} and from 0.53 to 0.64 x 10^5 cells m^{-3} at greater depths. The cell volume ranges from 0.049 to 0.098 µm^3, with a mean value of 0.072 ± 0.018 µm^3. In the photic and aphotic layers, the cell volumes vary in a similar range (0.08 ± 0.02 µm^3). The highest volumes at great depths characterise stations 30 and 10, where large, curved rods are observed. Apart from stations 30 and 10, the data show a similar vertical profile in the size distribution. The highest percentage of live cells (about 33%) is observed at station 46 in the photic layer. However, peaks are also found in the deeper layers. The number of respiring cells (CTC+) is in the order of 104 cells ml^{-1}. Variability between the layers is observed at all stations. In general, the high proportion of respiring cells below 100 m depth is observed at stations 46, 30 and 20. Conversely, the higher percentages are found in the photic layer at stations St. 10 and 1 (Fig. 12).
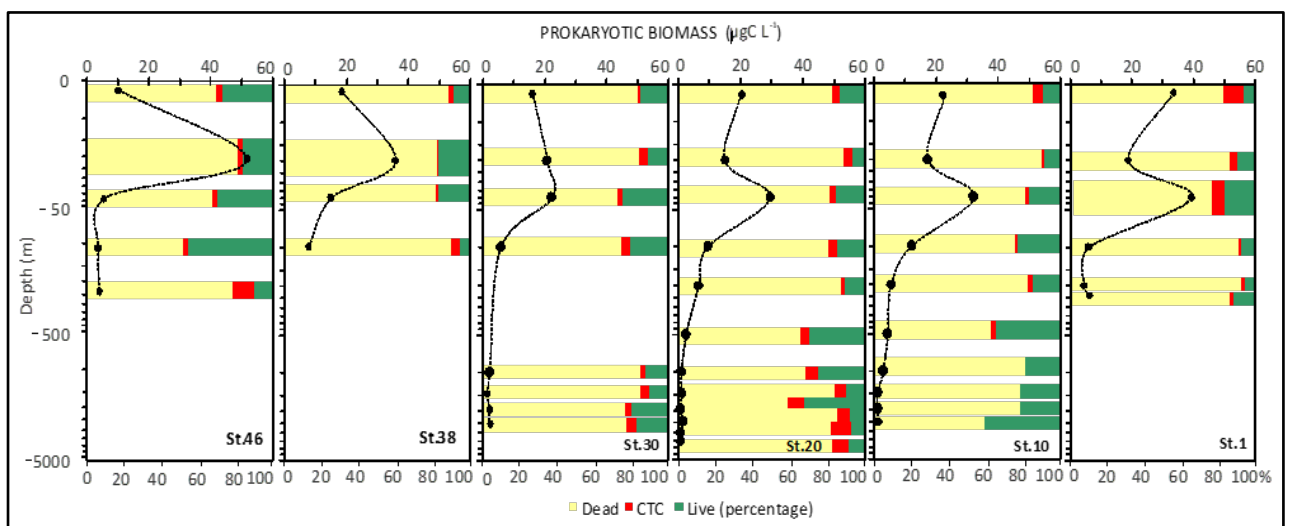
Figure 12 - Vertical profiles of prokaryotic biomass, viable and dead cells (Live/Dead) and respiring cells (CTC); Data on y axis are represented in natural log (*ln*) scale.

Overall, the average percentages of carbon source utilisation determined by Biolog Ecoplates show that carbohydrates and carboxylic acids were well-utilised polymers at each station and in each layer. Especially in the aphotic layer, the percentage utilisation is highest at most stations. Complex carbon sources and phosphate carbon are utilised at similar percentages throughout the water column; conversely, amino acids are preferentially utilised in the aphotic layer. Amines are only little used (Fig. 13).
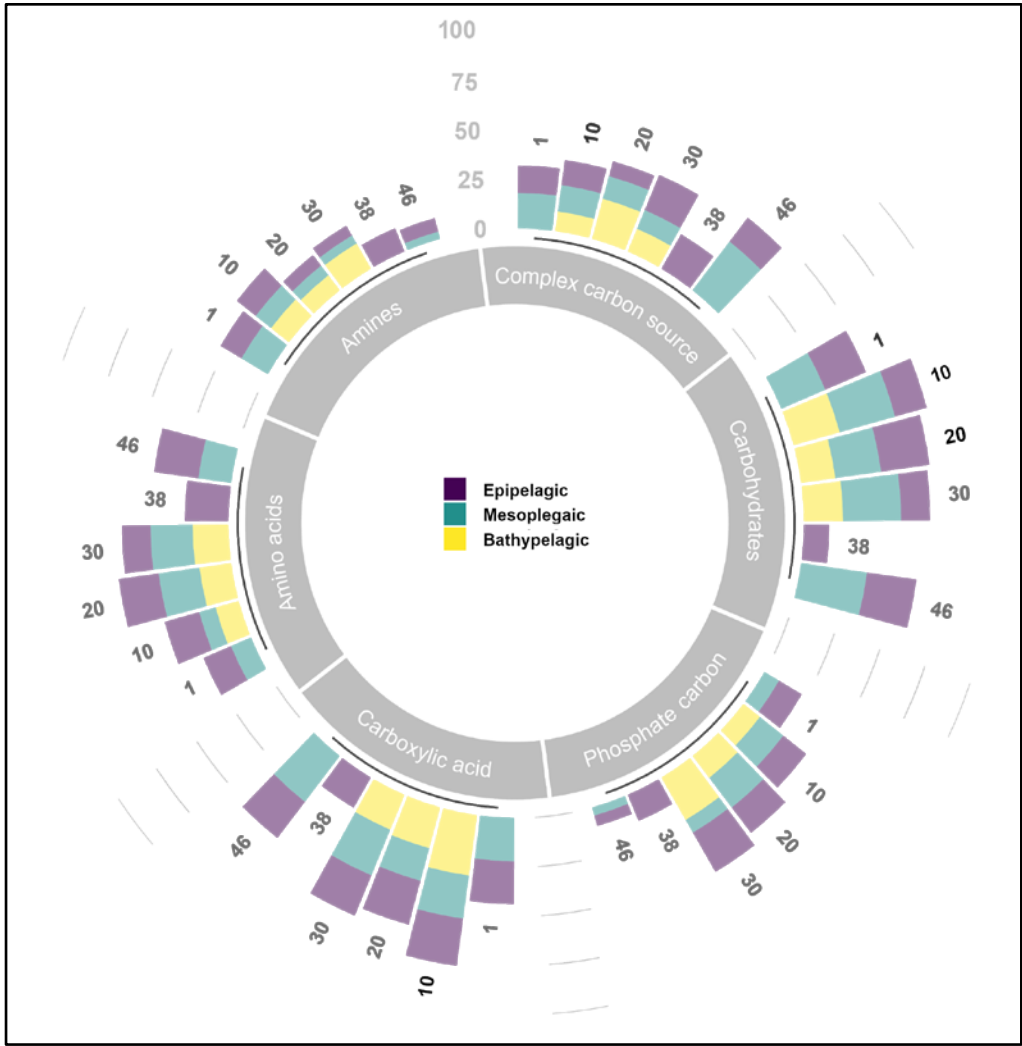
Figure 13 - Carbon substrate utilisation (as percentage of the total) determined in the epi-, meso-, and bathy-pelagic layers.

Enzymatic activity measurements yield values of LAP, GLU and AP ranging from 0.072 to 8.08 nM h^{-1}, from 0.007 to 0.35 nM h^{-1} and from 0.001 to 0.36 nM h^{-1} respectively (Fig. 14). Total enzymatic patterns depict vertical trends generally decreasing from surface towards deep layers, with some hot spots of metabolic activity at 20-40 m and in the aphotic layer. LAP activity peaks at the lateral ends of the transect as well as at St. 20. AP and GLU decrease from the Western (Greenland) side moving towards St 20, then increase again towards the Eastern side (St. 10) of the transect.
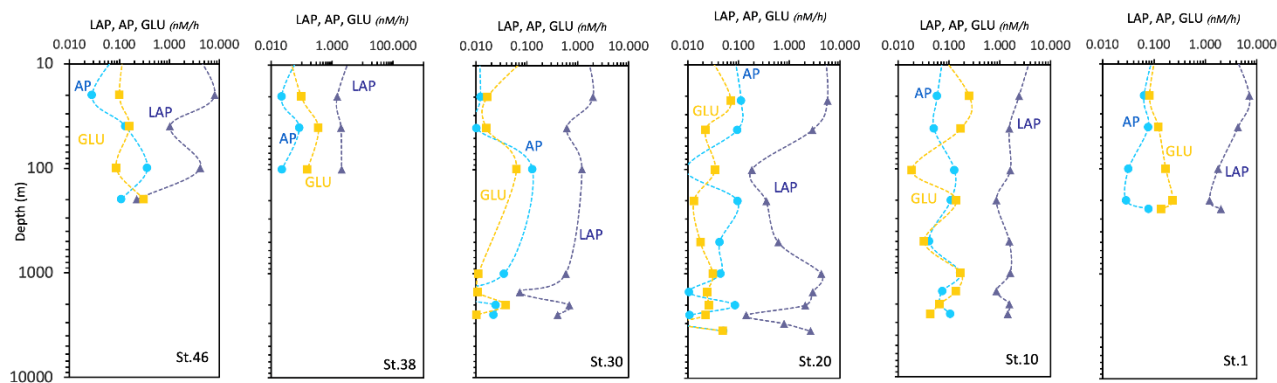
547
548 **Figure 14** - Vertical profiles of the enzymatic activity rates measured at the sampled stations (LAP, leucine
549 aminopeptidase; AP, alkaline phosphatase; GLU, beta glucosidase). Data are represented in natural log (*ln*) scale.
550

551 The respiration rates (ETS) range from 0.0290 to 0.329 µL O$_2$ h^{-1} L^{-1} (Fig. 15). The respiratory
552 activity values generally decrease from the surface down to 1000 m depth and then increase again
553 in the deep layer (below 1000 m depth). A high value of respiratory activity was also determined
554 in the deepest sample of St. 46.
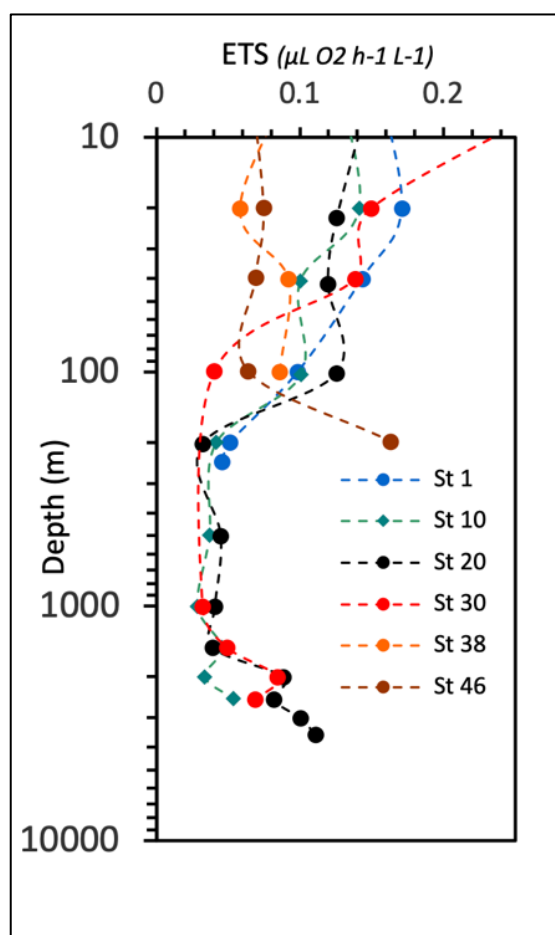
555
556 **Figure 15** - Vertical profiles of Electron Transport System (ETS) respiratory activity. Data on the y axis are
557 represented in natural log (*ln*) scale.

558

4 Summary and conclusions

Here we present the main data and results of the multidisciplinary oceanographic campaign carried out between 29 August and 14 September 2021 on board the Italian icebreaker Laura Bassi in the Greenland Sea (along the 75° N latitude section) as part of the Italian project CASSANDRA, funded by the Italian Ministry of Research in the framework of the Italian Arctic Programme. The Greenland Sea, in the north Atlantic, is a region of deep ocean convection that contributes to the AMOC and the exchange of water masses between the Atlantic and Arctic Oceans. On its easternmost side, it is dominated by the presence of AW, while on the westernmost side, by the presence of Polar waters. Both large scale patterns, local meteorological conditions, and ice extent can influence physical and biogeochemical properties. Different phases of the North Atlantic Oscillation index (NAO, i.e., atmospheric pressure difference between the Azores high and the subpolar low at sea level) can modulate basin-wide changes in the intensity and position of the North Atlantic jet stream and storm track, as well as influence patterns of zonal and meridional heat and moisture transport, which in turn can affect temperature and precipitation patterns over the Arctic and sub-Arctic regions. Increasingly positive phases of the NAO are associated with increased AW inflow, as was the case in the late 1980s/early 1990s (Dickson et al., 2000). The winter of 2020/2021, which preceded the cruise, had a slightly negative NAO index (-0.72), after two years of predominantly positive values. A negative NAO means weaker westerly winds in the mid-latitude regions in terms of climatology and stronger winds in the North Atlantic west of Iceland. Sea ice in the Fram Strait fluctuates from year to year. The lowest extent in September was recorded exactly in 2021, the highest in 1987. In the long term, the regions of the Norwegian Sea and the Fram Strait experienced a drop in temperature from 2018 to 2020, which rose again in 2021. Instead, a strong freshening phase set in after 2013, which is continuing. Continuous warming was also observed in the deep-water layer of the Greenland Sea at a depth of 3000 metres. In particular, the GSDW temperature shows a relatively steady increase from -1.18 °C to -0.86 °C between 1993 and 2021 (ICES Report on Ocean Climate 2021, available at https://ices-library.figshare.com/articles/report/ICES_Report_on_Ocean_Climate_2021/24755574?file=43769571). Our measurements report temperature values of about -0.9 °C for the GSDW. Relatively warm and saline Atlantic Water (AW, $\theta > 3.0$°C, S about 35), with highest A_T concentrations, dominates on the eastern side in the upper 500 m with surface temperatures of 4.5–9.0 °C. A dome-shaped isotherm distribution indicates upwelling from the Greenland Sea Gyre, while several mesoscale structures such as eddies seem to be responsible for the large spatial variability in the upper layer. At the surface, the central Greenland Sea is almost nutrient poor. On the western side, however, higher phosphate and silicate values are good indicators for the upper halocline of the Arctic surface water along the Greenland slope. Nitrate levels remained very low there. The deep waters NSDW and GSDW, presented the lowest pH_T values and the highest enrichment of silicate. Phytoplankton biomass along the euphotic water column, expressed as chl-*a*, showed a quali-quantitative difference between the central-eastern and western sectors with greater abundances at the extremes of the transect. The dimensional structure of the phytoplankton community characterizes the PW with a predominance of the micro-phytoplankton fraction that almost entirely replaces the nano-phytoplankton fraction, more abundant in the AW, even in the front station between these two water masses. The plankton communities were analysed with more detail in the upper layer (0-100 m), where the phytoplankton and zooplankton diversity reflected the different water masses (AW and PW). Diatoms increased at the western stations affected by PW, while dinoflagellates and small

flagellates were more abundant at the eastern stations affected by AW. The higher MZP abundance was recorded at St. 38, where the layer below 30-40 m depth was still occupied by AW, while the surface layer was affected by PW. The MZP abundance and biomass decreased drastically in the presence of cold PW on the Greenland slope. Micrometazoans and aloricate ciliates increased towards the easternmost side of the section, where the stations were characterised by higher temperatures. Copepods of the genus *Calanus* were the main taxa observed, but the structure of the mesozooplankton communities changed along the transect and polar taxa increased westwards. The $\delta^{18}O$ and δD isotope ratios indicate the influence of freshwater at the surface level near the Greenland shelf. We also highlight a marked difference in $\delta^{18}O$ and δD isotope ratios between GSDW and NSDW, which occupies the bottom region of the studied area, with NSDW showing lower values compared to GSDW. Prokaryotic abundance and microbial enzymes generally depicted vertical decreasing trends with peaks of cells and activity recorded at station 20 as well as at the ends of the transect. While living cells prevailed at station 46 in the photic layer, actively respiring cells were quite variable in their distribution. Large, curved rods were found at stations 30 and 10. A high utilization of carbohydrates and carboxylic acids regardless of the examined station or depth characterized the microbial community metabolism. Amino acids were actively metabolised in the aphotic layer, while no differences were found in the utilization of complex carbon sources and phosphate carbon compounds along the water column.

This study emphasises the significant spatial and vertical variability of water properties, nutrient distribution and biological communities caused by local and seasonal oceanographic dynamics in a region characterised by a strong exchange of water masses between the Arctic and Atlantic Oceans and a major influence of atmospheric teleconnections between the polar and subpolar regions.

5 Data availability

Data presented here are available through the repository Italian Arctic Data Center (IADC), at the following links: CTD casts, available at https://doi.datacite.org/dois/10.71761%2Fc082c3ca-40bf-42b1-a61a-7b3697ab2c5a (Bensi et al., 2024). Physical, biological, and biogeochemical analyses on water samples from Niskin bottles available at https://doi.datacite.org/dois/10.71761%2Ff7474404-3331-43e5-883b-25755e94956d (Azzaro et al., 2024). Satellite data used in the work are freely available at https://worldview.earthdata.nasa.gov/. Data on sea ice extension are available at https://mosj.no/en/indikator/climate/ocean/sea-ice-extent-in-the-barents-sea-and-fram-strait/.

Declaration of Competing Interest

The authors declare that they have no known competing financial interests or personal relationships that could have appeared to influence the work reported in this paper.

Acknowledgements

The field activities carried out on board the icebreaker Laura Bassi were partly funded by the Italian Ministry of University and Research through the Italian Arctic Research Programme (https://www.programmaricercaartico.it/), the National Institute of Oceanography and Applied Geophysics (OGS) and the National Research Council (CNR). The research was conducted as part of the project "AdvanCing knowledge on the presentArctic Oceanby chemical-phySical,

biogeochemical and biological obServAtioNs to preDict the futuRe chAnges" (CASSANDRA), which was funded by the Italian Arctic Research Programme (CASSANDRA project; PRA21_0001). This study was supported by the Synoptic Arctic Survey (SAS) – an international research programme that coordinates the data collection of essential ocean variables measured during Arctic research cruises. SAS is partly funded by the European Union's Horizon 2020 research and innovation programme through the Arctic PASSION project under the grant agreement 10100347. We would also like to thank Lidia Urbini, Paolo Mansutti, Leonardo Langone, Patrizia Giordano, Warren Cairns, Matteo Feltracco, the entire technical staff of the OGS, the captain and crew of the Laura Bassi for their support during the data collection. We also thank Alenka Goruppi and Giulia Peloso (OGS, Trieste, Italy) for their help in processing the zooplankton data and Nives Ogrinc (Jožef Stefan Institute Ljubljana, Slovenia) for the analyses of δ13C-DIC.

Author contribution

M.B., M.A. and G.Ci. conceived and wrote the main part of the article. M.B., M.A., G.Ci., M.G., V.K., C.R, M.M, T.D., F.R., M.K., A.L.G., V.T., E.P., A.d.O., D.B., F.C., A.C.R., M.P., G.Ca., G.M., C.T., L.P. F.S., F.D., C.C. contributed to the collection and/or processing of the data, preparation of figures, and to the discussion of the results. M.A. led the CASSANDRA project. All authors have contributed to the preparation and revision of the final version of the manuscript.

References

Ahme, A., Von Jackowski, A., McPherson, R. A., Wolf, K. K. E., Hoppmann, M., Neuhaus, S. and John, U.: Winners and Losers of Atlantification: The Degree of Ocean Warming Affects the Structure of Arctic Microbial Communities, Genes, 14, 623. https://doi.org/10.3390/genes14030623, 2023.

Andersen, P., and Throndsen, J.: Estimating cell numbers, in: Manual on Harmful Marine Microalgae, edited by: Hallegraeff, G. M., Anderson, D. M., and Cembella, A., Monographs on Oceanographic Methodology, Unesco Publishing, Paris, France, 11, 99–130, 2004.

Anderson, L. G., Drange, H., Chierici, M., Fransson, A., Johannessen, T., Skjelvan, I, Rey, F.: Annual carbon fluxes in the upper Greenland Sea based on measurements and a box-model approach. Tellus, 52B, 1013-1024, 2000.

Azzaro, M., Specchiulli, A., Maimone, G., Azzaro, F., Lo Giudice, A., Papale, M., La Ferla, R., Paranhos, R., Souza Cabral, A., Rappazzo, A. C., et al.: Trophic and Microbial Patterns in the Ross Sea Area (Antarctica): Spatial Variability during the Summer Season. J. Mar. Sci. Eng. 10, 1666. https://doi.org/ 10.3390/jmse10111666, 2022.

Azzaro M., Aliani S., Maimone, G., Decembrini F., Caroppo C., Giglio F., Langone L., Miserocchi S., Cosenza A., Azzaro F., et al.: Short-term dynamics of nutrients, planktonic abundances and microbial respiratory activity in the Arctic Kongsfjorden (Svalbard, Norway). Polar Biol. 44, 361–378, 2021.

Azzaro, M., Bensi, M., Civitarese, G., et al. CTD (data from NISKIN Bottles) LB21 ARCTIC Cruise Italian Arctic project CASSANDRA [Data set]. ISP-CNR. https://doi.org/10.71761/F7474404-3331-43E5-883B-25755E94956D, 2024.

Azzaro, M., La Ferla, R., and Azzaro, F.: Microbial respiration in the aphotic zone of the Ross Sea (Antarctica), Mar. Chem., 99(1), 199-209, https://doi.org/ 10.1016/j.marchem.2005.09.011, 2006.

Babb, D. G., Galley, R. J., Kirillov, S., Landy, J. C., Howell, S. E. L., Stroeve, J. C., Meier, W., Ehn, J. K., and Barber, D. G.: The stepwise reduction of multiyear sea ice area in the Arctic Ocean since 1980, J. Geophys. Res. Oceans, 128, 10, https://doi.org/10.1029/2023JC020157, 2023.

Beers, J. R., and Stewart, G. L.: Numerical abundance and estimated biomass of microzooplankton, in: The ecology of the plankton off La Jolla, California, in the period April through September 1967, edited by: Strickland, J. D. H., University of California Press, Berkeley, USA, 67–87, 1970.

Bensi, M., Kovacevic, V., & Mansutti, P.: CTD (DOWNCAST) LB21 ARCTIC Cruise Italian Arctic project CASSANDRA [Data set]. IADC. https://doi.org/10.71761/C082C3CA-40BF-42B1-A61A-7B3697AB2C5A, 2024.

Brakstad, A., K. Våge, L. Håvik, and G. W. K. Moore: Water Mass Transformation in the Greenland Sea during the Period 1986–2016. J. Phys. Oceanogr., 49, 121–140, https://doi.org/10.1175/JPO-D-17-0273.1, 2019.

Carmack, E., Polyakov, I., Padman, L., Fer, I., Hunke, E., Hutchings, J., Jackson, J., Kelley, D., Kwok, R., Layton, C., Melling, H., Perovich, D., Persson, O., Ruddick, B., Timmermans, M., Toole, J., Ross, T., Vavrus, S., & Winsor, P.: Toward Quantifying the Increasing Role of Oceanic Heat in Sea Ice Loss in the New Arctic. Bull. of the Am. Met. Society, 96(12), 2079-2105, https://doi.org/10.1175/BAMS-D-13-00177.1, 2015.

Carpenter, J. H.: The accuracy of the Winkler method for dissolved oxygen analysis. Limnol. Oceanogr., 10, 135–140, https://doi.org/10.4319/lo.1965.10.1.0135, 1965.

Carter-Gates, M., Balestreri, C., Thorpe, S. E., Cottier, F., Baylay, A., Bibby, T. S., et al.: Implications of increasing Atlantic influence for Arctic microbial community structure, Sci. Rep., 10, 19262, https://doi.org/10.1038/s41598-020-76293-x, 2020.

Caruso, G., La Ferla, R., Azzaro, M., Zoppini, A., Marino, G., Petochi, T., et al.: Microbial assemblages for environmental quality assessment: knowledge, gaps and usefulness in the European Marine Strategy Framework Directive, Crit. Rev. Microbiol., 42, 883–904, https://doi.org/10.3109/1040841X.2015.1087380, 2016.

Caruso, G., Madonia, A., Bonamano, S., Miserocchi, S., Giglio, F., Maimone, G., et al.: Microbial abundance and enzyme activity patterns: response to changing environmental characteristics along a transect in Kongsfjorden (Svalbard Islands), J. Mar. Sci. Eng., 8, 824, https://doi.org/10.3390/jmse8100824, 2020.

Chatterjee, S., Raj, R. P., Bertino, L., Skagseth, Ø., Ravichandran, M., and Johannessen, O. M.: Role of Greenland Sea Gyre Circulation on Atlantic Water Temperature Variability in the Fram Strait, Geophys. Res. Lett., 45, 8399–8406, https://doi.org/10.1029/2018GL079174, 2018.

Clarke, R., Swift, J., Reid, J., and Koltermann, K.: The formation of Greenland Sea Deep Water: double diffusion or deep convection? Deep Sea Res. Part A, Oceanogr. Res. Pap., 37, 1385-1424 https://doi.org/10.1016/0198-0149(90)90135-I, 1990.

Csapó, H. R., Grabowski, M., and Węsławski J.M.K.: Coming home - Boreal ecosystem claims Atlantic sector of the Arctic, Sci. Total Environ., 771, 144817, https://doi.org/10.1016/j.scitotenv.2020.144817, 2021.

Decembrini, F., Caroppo C., Caruso, G., and Bergamasco, A.: Linking microbial functioning and trophic pathways to mesoscale processes and ecological status in a coastal ecosystem: Gulf of Manfredonia (south Adriatic Sea), Water, 13, 1325. https://doi.org/10.3390/w13091325, 2021.

Dickson, R. R., Osborn, T. J., Hurrell, J. W., Meincke, J., Blindheim, J., Adlandsvik, B., et al.: The Arctic Ocean Response to the North Atlantic Oscillation, J. Climate, 13, 2671–2696, https://doi.org/10.1175/1520-0442(2000)013<2671:TAORTT>2.0.CO;2, 2000.

732 de Steur, L., Sumata, H., Divine, D.V., et al. Upper ocean warming and sea ice reduction in the East
733   Greenland Current from 2003 to 2019. Commun Earth Environ 4, 261.
734   https://doi.org/10.1038/s43247-023-00913-3, 2023.

735 Dukhovskoy, D. S., Yashayaev, I., Proshutinsky, A., Bamber, J. L., Bashmachnikov, I. L.,
736   Chassignet, E. P., et al.: Role of Greenland freshwater anomaly in the recent freshening of the
737   subpolar North Atlantic. J. Geophys. Res. Oceans, 124, 3333–3360,
738   https://doi.org/10.1029/2018JC014686, 2019.

739 Edler, L.: Recommendations for marine biological studies in the Baltic Sea. Phytoplankton and
740   chlorophyll. Baltic Mar. Biol., 5, 1-37, 1979.

741 Fan, H., Borchert, L.F., Brune, S., Koul, V., and Baehr, J.: North Atlantic subpolar gyre provides
742   downstream ocean predictability, npj Clim. Atmos. Sci., 6, 145, https://doi.org/10.1038/s41612-
743   023-00469-1, 2023.

744 Fransner F., Fröb F., Tjiputra J. , Goris N., Lauvset S. K., Skjelvan I., Jeansson E., Omar A., Chierici
745   M., Jones E., Fransson A., Ólafsdóttir S. R., Johannessen T., Olsen A.: Acidification of the
746   Nordic Seas, Biogeosciences, 19, 979–1012, https://doi.org/10.5194/bg-19-979-2022, 2022.

747 Grasshoff, K., Kremling, K., and Ehrhardt, M.: Methods of Seawater Analysis, Wiley-VCH,
748   Weinheim, 600 pp., 1999.

749 Hansen, H. P., and Koroleff, F.: Determination of nutrients, in: Methods of Seawater Analysis, 3rd
750   Edn., edited by: Grasshoff, K., Kremling, K., and Ehrhardt, M., Wiley-VCH, Weinheim, 159–
751   228, https://doi.org/10.1002/9783527613984.ch10, 1999.

752 Hoppe, H. G.: Use of fluorogenic model substrates for extracellular enzyme activity (EEA)
753   measurement of bacteria, 1st edition, In: Handbook of methods in aquatic microbial ecology,
754   edited by: Kemp, P. F., Sherr, B. F., Sherr, E. B., and Cole, J. J., Lewis Publisher, Boca Raton,
755   FL-USA, 423-432, https://doi.org/10.1201/9780203752746, 1993.

756 Ingrosso, G., Giani, M., Comici, C., Kralj, M., Piacentino, S., De Vittor, C., Del Negro, P.: Drivers
757   of the carbonate system seasonal variations in a Mediterranean gulf. Estuar. Coast. Shelf Sci.
758   168, 58-70, https://doi.org/10.1016/j.ecss.2015.11.001, 2016a.

759 Ingrosso, G., Giani, M., Cibic, T., Karuza, A., Kralj, M., Del Negro, P.: Carbonate chemistry
760   dynamics and biological processes along a river–sea gradient (Gulf of Trieste, northern Adriatic
761   Sea). J.Mar. Syst. 155, 35–49. http://dx.doi.org/10.1016/j.jmarsys.2015.10.013, 2016b.

762 Ingvaldsen, R.B., Assmann, K.M., Primicerio, R., et al.: Physical manifestations and ecological
763   implications of Arctic Atlantification. Nat Rev Earth Environ 2, 874–889.
764   https://doi.org/10.1038/s43017-021-00228-x, 2021.

765 La Ferla, R., Maimone, G., Azzaro, M., Conversano, F., Brunet, C., Cabral, A.S., Paranhos, R.:
766   Vertical distribution of the prokaryotic cell size in the Mediterranean Sea. Helgol. Mar. Res. 66,
767   635–650. https://doi.org/10.1007/s10152-012-0297-0, 2012.

Noji T.T., Rey F., Miller L.A., Borsheim K. Y., Urban-Rich J.: Fate of biogenic carbon in the upper 200 m of the central Greenland Sea. Deep-Sea Res. II 46, 1497-1509, https://doi.org/10.1016/S0967-0645(99)00032-6, 1999.

Norwegian Polar Institute: Sea ice extent in the Fram Strait in September. Environmental monitoring of Svalbard and Jan Mayen (MOSJ). URL: http://mosj.no/en/climate/ocean/sea-ice-extent-barents-sea-fram-strait.html (https://mosj.no), 2022.

Onarheim, I. H., Årthun, M., Teigen, S. H., Eik, K. J., & Steele, M.: Recent Thickening of the Barents Sea ice cover. GRL, 51, e2024GL108225. https://doi.org/10.1029/2024GL108225, 2024.

Oudot, C., Gerard, R., Morin, P., Gningue, I.: Precise shipboard determination of dissolved oxygen (Winkler procedure) for productivity studies with commercial system. Limnol. Oceanogr. 33, 146–150,https://doi.org/10.4319/lo.1988.33.6part2.1646, 1998.

Pettine, M., Capri, S., Manganelli, M., Patrolecco, L., Puddu, A., and Zoppini, A.: The Dynamics of DOM in the Northern Adriatic Sea. Estuarine, Coastal and Shelf Science, 52, 471–489, https://doi.org/10.1006/ecss.2000.0752, 2001.

Polyakov, I. V., Ingvaldsen, R. B., Pnyushkov, A. V., Bhatt, U. S., Francis, J. A., and Janout, M., et al.: Fluctuating Atlantic inflows modulate Arctic Atlantification, Science, 381, 972-979, https://doi.org/10.1126/science.adh5158, 2023.

Polyakov, I. V., et al.: Greater role for Atlantic inflows on sea-ice loss in the Eurasian Basin of the Arctic Ocean. Science 356, 285-29 1. DOI:10.1126/science.aai8204, 2017.

Postel, L., Fock, H., and Hagen, W.: Biomass and abundance, ICES Zooplankton Meth. Manual, 83–192, https://doi.org/10.1016/B978-012327645-2/50005-0, 2000.

Priest, T., von Appen, WJ., Oldenburg, E., Popa, O., Torre-Valdés, S., Bienhold, C., et al.: Atlantic water influx and sea-ice cover drive taxonomic and functional shifts in Arctic marine bacterial communities. ISME J., 17, 1612–1625, https://doi.org/10.1038/s41396-023-01461-6, 2023.

Putt, M., and Stoecker, D. K.: An experimentally determined carbon: volume ratio for marine "oligotrichous" ciliates from estuarine and coastal waters, Limnol. Oceanogr., 34, 1097-1107, https://doi.org/10.4319/lo.1989.34.6.1097, 1989.

Rantanen, M., Karpechko, A.Y., Lipponen, A. et al.: The Arctic has warmed nearly four times faster than the globe since 1979. Commun Earth Environ 3, 168. https://doi.org/10.1038/s43247-022-00498-3, 2022.

Relitti, F., Ogrinc, N., Giani, M., Cerino, F., Smodlaka Tankovic, M., Baricevic, A., Urbini, L., Krajnc B., Del Negro, P., De Vittor, C.: Stable carbon isotopes of phytoplankton as a tool to monitor anthropogenic CO_2 submarine leakages. Water, 12, 3573. https://doi.org/10.3390/w12123573, 2020.

803 Rudels, B., Friedrich, H. J., Quadfasel, D.: The Arctic Circumpolar Boundary Current, Deep-Sea
804   Res. Part II, 46, 1023-1062, https://doi.org/10.1016/S0967-0645(99)00015-6, 1999.

805 Schlitzer, R.: Ocean Data View, https://odv.awi.de, 2024.

806 Simpkins, G.: Greenland Sea convection. Nature Clim Change 9, 7. https://doi.org/10.1038/s41558-
807   018-0384-6, 2019.

808 Skjelvan, I., Olsen, A., Anderson, L. G., Bellerby, R. G. J., Falck, E, Kasajima, Y., Kivimäe, C.,
809   Abdirahman, O., Rey, F., Olsson, K. A., Johannessen, T., Heinze, C. A review of the inorganic
810   carbon cycle of the Nordic Seas and Barents Sea. In: Drange H. et al. (Eds.) The Nordic Seas:
811   An Integrated Perspective Oceanography, Climatology, Biogeochemistry, and Modeling.,
812   Geophys. Monogr. Ser., vol. 158, pp. 157-175, AGU, Washington, D. C. 2005.

813 Smedsrud, L. H., Muilwijk, M., Brakstad, A., Madonna, E., Lauvset, S. K., Spensberger, C., etal.:
814   Nordic Seas Heat Loss, Atlantic Inflow, and Arctic Sea Ice Cover Over the Last Century, Rev.
815   Geophys., 60, https://doi.org/10.1029/2020RG000725, 2022.

816 Throndsen, J.: Preservation and Storage, in: Phytoplankton Manual, edited by: Sournia, A., Unesco
817   Publishing, Paris, France, 69–74, 1978.

818 Urbini, L., Ingrosso, G., Djakovac, T., Piacentino, S., Giani, M.: Temporal and Spatial Variability
819   of the CO_2 System in a Riverine Influenced Area of the Mediterranean Sea, the Northern
820   Adriatic. Front. Mar. Sci., 679, https://doi.org/10.3389/fmars.2020.00679, 2020.

821 Utermöhl, H.: Zur Vervollkommung der quantitativen Phytoplankton-Methodik. Mitt Int Ver Theor
822   Angew Limn, 9, 1-38, 1958.

823 van Guelpen, L., Markle, D. F., and Duggan, D. J.: An evaluation of accuracy, precision, and speed
824   of several zooplankton subsampling techniques, ICES J. Mar. Sci., 40, 226–236,
825   https://doi.org/10.1093/icesjms/40.3.226, 1982.

826 Verity, P. G., Lagdon, C.: Relationship between lorica volume, carbon, nitrogen, and ATP content
827   of tintinnids in Narragansett Bay, J. Plankton Res., 6, 859-868,
828   https://doi.org/10.1093/plankt/6.5.859, 1984.

829 von Bodungen, B., Antia, A., Bauerfeind, E. et al.: Pelagic processes and vertical flux of particles:
830   an overview of a long-term comparative study in the Norwegian Sea and Greenland Sea. Geol.
831   Rundsch. 84, 11–27, https://doi.org/10.1007/BF00192239, 1995.

832 Wang, X., Zhao, J., Hattermann, T., Lin, L., & Chen, P.: Transports and accumulations of Greenland
833   Sea intermediate waters in the Norwegian Sea. Journal of Geophysical Research: Oceans, 126,
834   e2020JC016582. https:// doi.org/10.1029/2020JC016582, 2021.

835 Whitt, D. B.: Global Warming Increases Interannual and Multidecadal Variability of Subarctic
836   Atlantic Nutrients and Biological Production in the CESM1-LE, Geophys. Res. Lett., 50,
837   https://doi.org/10.1029/2023GL104272, 2023.

838   Yergeau, E., Michel, C., Tremblay, J., Niemi, A., King, T. L., Wyglinski, J., et al.: Metagenomic
839   survey of the taxonomic and functional microbial communities of seawater and sea ice from the
840   Canadian Arctic, 10.1038/srep42242, Sci. Rep., 7, 42242, 2017.

841   Zingone., A., Totti, C., Sarno, D., Cabrini, M., Caroppo, C., Giacobbe, M. G., Lugliè, A., Nuccio,
842   C., and Socal, G. Fitoplancton: metodiche di analisi quali-quantitativa, in: Metodologie di studio
843   del plancton marino, edited by: Socal, G., Buttino, I., Cabrini, M., Mangoni, O., Penna, A., and
844   Totti, C., Manuali e Linee Guida ISPRA SIBM, Rome, Italy, 213–237, 2010.